Doctoral Dissertation

Ultrasonic phased array imaging with waveguide buffer

ウェーブガイドバッファを用いた超音波フェーズドアレイイメージング

Xia Mingqian

July 2025

Graduate School of Engineering
The University of Osaka

Abstract

Maintenance and quality control are essential for ensuring the safety, performance, and longevity of industrial facilities and infrastructure. In sectors such as energy, aerospace, and transportation, components are often subjected to severe conditions including thermal stress, mechanical loads, and corrosion. These factors can lead to degradation mechanisms such as fatigue and stress corrosion cracking (SCC), especially in critical regions like heat affected zones (HAZs) near welds. To prevent structural failures and extend service life, nondestructive testing (NDT) techniques are widely used to detect defects without damaging the components. Among the available inspection techniques, ultrasonic phased array (PA) technology is widely employed in NDT. However, in high temperature environments such as nuclear power plants, direct contact between probes and test objects is often impractical. Buffer rods are typically used to transmit ultrasonic signals while protecting the probe from heat. However, conventional bulk buffer rods suffer from near field limit that degrade beamforming performance when used with PA probes. This thesis proposes an alternative solution using waveguide-based buffer designs, inspired by guided wave behavior in plates and cylinders. Focusing on pipelines that carry high temperature liquid sodium coolant, this study explores waveguide buffers that preserve effective PA inspection under high temperature conditions.

First, numerical analyses were conducted to investigate PA imaging using a stacked plate buffer. The buffer was designed based on the dispersion characteristics of the S0 mode in Lamb waves to maintain the performance of the phased array transducer. Initial simulations showed limitations in imaging quality due to multiple reflections at the buffer ends. The concept of the effective detecting region (EDR) for a PA probe with a stacked plate buffer was then established through theoretical derivation and validated by numerical simulations. Results confirmed agreement between theory and simulation, and further analyses demonstrated that increasing the buffer length extends the EDR.

Second, experimental investigations were conducted to evaluate the feasibility of PA imaging using a stacked plate buffer. A buffer was fabricated based on the S0 mode dispersion characteristics and tested in defect imaging experiments. The initial results showed high intensity spurious regions and blurred defect images. Subsequent numerical analysis indicated that these spurious images were caused by trailing waves generated in a plate. Theoretical and numerical studies demonstrated that increasing the plate width can remove these trailing waves. Experiments with wider plates confirmed that the

spurious images were effectively removed, resulting in clearer defect images.

Finally, to further solve the problems of trailing waves in plates, a buffer consisting of a bundle of circular cylinders was developed. The design was determined by considering the dispersion characteristics of the longitudinal guided wave modes in circular cylinders and parameters of the PA probe. In experiments using the buffer consisting of a bundle of circular cylinders, defects were successfully imaged using two imaging algorithms as plane wave imaging and total focusing method even though with a relatively small signal-to-noise ratio. The influences of trailing waves happened in stacked plate buffer were successfully solved by a buffer consisting of a bundle of circular cylinders with small diameter.

Table of contents

List of abbreviations

Abbreviation	Definition
A0	Zero-order Antisymmetric (mode of Lamb wave)
A1	First-order Antisymmetric (mode of Lamb wave)
EDR	Effective Detecting Region
EMAT	Electromagnetic Acoustic Transducer
ET	Electromagnetic Testing
FEM	Finite Element Method
FMC	Full Matrix Capture
HAZ	Heat Affected Zone
MPT	Magnetic Particle Testing
NDT	Non-Destructive Testing
PA	Phased Array
PAUT	Phased Array Ultrasonic Testing
PDE	Partial Differential Equation
PWI	Plane Wave Imaging
ROI	Region Of Interest
RT	Radiography Testing
S0	Zero-order Symmetric (mode of Lamb wave)
S1	First-order Symmetric (mode of Lamb wave)
SAFE	Semi-Analytical Finite Element
SCC	Stress Corrosion Crack
SDH	Side Drilled Hole
SH	Shear Horizontal
SNR	Signal to Noise Ratio
SUS	Steel Use Stainless
TFM	Total Focusing Method
UT	Ultrasonic Testing
UV	Ultraviolet

Chapter 1 Introduction

1.1 Research background

Maintenance and quality control are fundamental aspects of ensuring safety, efficiency, and reliability across a wide range of industrial sectors and infrastructure systems. Industrial facilities such as chemical plants, power plants, and steel plants, as well as civil structures like bridges, are subject to continuous mechanical loads, thermal stress, corrosion, and environmental exposure. Over time, these factors can lead to material degradation, fatigue cracking, wall thinning, and other structural issues. As a result, routine maintenance and periodic inspections are essential to detect early signs of damage, prevent catastrophic failures, and extend the service life of critical components [1-4].

Similarly, airplanes and automobiles require strict quality control during manufacturing and throughout their service life. In the aerospace and automotive industries, even minor defects can lead to severe consequences, making it imperative to ensure that components meet strict design and safety standards. Quality control measures include precise dimensional inspections, material testing, and defect evaluation to guarantee performance and integrity under operating conditions [5-11].

Across all these applications, Nondestructive Testing and Evaluation (NDT/NDE) has become a key method of effective maintenance and quality control. NDT and NDE refer to the evaluation of materials or components for surface or internal flaws without compromising their integrity or suitability for service. They involve inspecting and characterizing defects in accordance with established standards, without altering the original properties or causing damage to the tested object. NDT techniques offer a cost-effective approach for both targeted inspections and large-scale quality control, whether applied to individual components or entire production systems [12-15].

NDT is applied across a wide range of industries. In the aerospace sector, NDT plays a critical role in manufacturing, in-service inspection, and maintenance. It is commonly used to detect delamination, disbonding, and cracking in aircraft wings and other components subjected to high loads, harsh environments, and strict safety requirements. In transportation, NDT is widely used in railways, mass transit systems, and the automotive industry to evaluate the integrity of structural components, wheels, welds, and other critical parts for fatigue, corrosion, and cracks. For example, early

detection of rail defects through NDT can prevent track failure and ensure safe operation along entire railway lines. In construction, NDT contributes to the safety of infrastructure such as bridges, high-rise buildings, and dams by supporting structural health monitoring, aging assessments, and post-disaster inspections. In manufacturing, it is essential for quality control and continuous improvement of products. In the energy industry, particularly in the transportation and storage of oil and gas, as well as in nuclear power plants, NDT is indispensable for the inspection of pipelines, pressure vessels, and other safety-critical components during both construction and operation [16-20].

There are various types of NDT, including visual testing (VT), which involves direct observation of a component to identify surface discontinuities and is particularly effective for detecting macroscopic defects. Radiography testing (RT), a method based on the differential absorption of penetrating radiation, such as X-rays or gamma rays, by the material under inspection. Electromagnetic testing (ET), which involves inducing electric currents, magnetic fields, or both within a test object and observing the resulting electromagnetic response. Magnetic particle testing (MPT), which is a method used to detect surface and near-surface discontinuities in ferromagnetic materials by applying a magnetic field and observing the accumulation of magnetic particles at defect locations [21-27].

In this thesis, ultrasonic testing (UT) is applied in the research. UT is a nondestructive technique used to detect internal and surface defects in sound-conducting materials. It is one of the primary methods employed in this thesis. Various forms of UT are used in practice, including conventional ultrasonic testing and phased array ultrasonic testing (PAUT) [28-30].

Conventional UT is widely used NDT technique that utilizes ultrasonic waves to detect internal defects, measure thickness, and evaluate material properties. Typically, a piezoelectric transducer generates ultrasonic pulses that propagate through a medium and reflect from interfaces or discontinuities. Coupling is usually achieved via a gel or fluid to facilitate acoustic transmission. A notable implementation is the water immersion ultrasonic microscope, which immerses both the transducer and specimen in water to achieve precise acoustic coupling and high-resolution imaging of microstructural features, particularly in thin or delicate materials. Another important variant is the electromagnetic acoustic transducer (EMAT), which induces ultrasonic waves directly in conductive materials via electromagnetic interactions, eliminating the need for a coupling medium. EMAT is particularly able to use for high-temperature or surface-sensitive inspections [31-38].

Phased array ultrasonic testing differs from conventional UT in that it uses

multiple small piezoelectric elements arranged in specific patterns—such as linear, matrix, annular, or circular arrays—within a single probe. Each element can be excited independently with controlled timing (phasing), allowing the ultrasonic beam to be electronically steered and dynamically focused without physically moving the probe. Over the past several decades, PAUT has undergone significant development, leading to various probe designs and advanced techniques for data acquisition and signal analysis. These capabilities make PAUT especially useful for complex inspections requiring high resolution and adaptability [39-47].

This thesis focuses on the safety of nuclear power plant. The cooling system is a critical component of a nuclear power plant, essential for maintaining safe operation. During reactor operation, a significant amount of heat is generated by nuclear reactions. If not properly managed, this heat can lead to excessive temperature rises, potentially damaging the reactor system and resulting in catastrophic consequences. The coolant thus acts as a safeguard, removing heat from the reactor core and maintaining the system within safe temperature limits to ensure overall reactor integrity. In this thesis, our research is relating to safety inspection of the pipeline system of nuclear power plants. Pipeline is a kind of important system in the nuclear power plant to transport liquid or gas materials. For instance, cooling liquid for keeping the temperature of the reactor stable is often transmitted by pipes. Many pipes are stretched throughout the plant and some kinds of failures can occur in pipes depending on the type of content and changes in pressure. Failure mechanisms of pipes including stress corrosion, erosion, fatigue, construction errors, etc. Among these mechanisms, stress corrosion is relatively often found in failure accidents [48-50].

When connecting the pipes, welding is always used in engineering practice. Shown in Fig. 1.1, when the welding is applied to the pipes, heat affected zone (HAZ) will appear near the welding area. The HAZs near welds in pipes are often the starting point of pipe collapse due to stress corrosion crack (SCC). In the inspection of HAZs in nuclear power plants, for example, ultrasonic inspection is used to precisely locate the crack tip position to assess the remaining service life in consideration of the operating environment. In this thesis, we consider the pipes transmitting the liquid sodium coolant with working temperature of around 380-550℃. In this temperature, the object to be tested cannot be directly contacted by ultrasonic transducer [51-59].

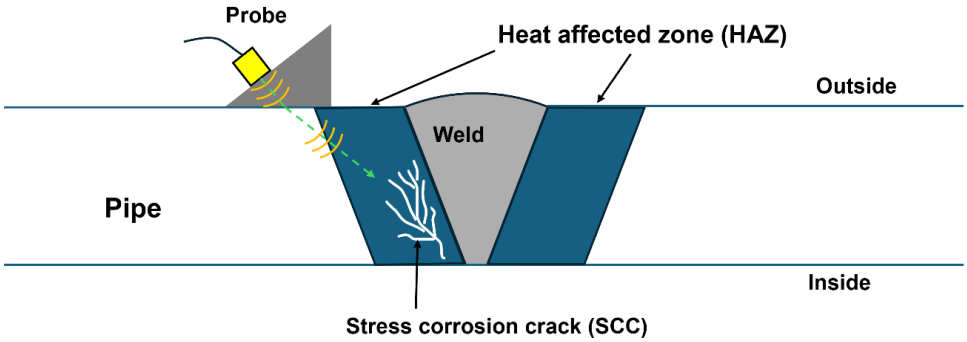

Figure 1.1: Schematic of ultrasonic testing of nuclear power plant pipes

For solving the problems happening in the high temperature testing, many methods come up like high temperature transducer, laser ultrasonic testing, air coupled ultrasonic testing and buffer rod method. Among these methods, buffer method can be simpler and cheaper than other methods. This method can be used to connect a normal transducer and the testing object to both transmit the signal through the buffer and keep the transducer away from the high temperature environment which the testing object is surrounded by [60,61].

However, when a PA probe is used in combination with a bulk buffer rod, the near-field limit imposes a constraint on the effective detection range. Early beam focusing occurs within the buffer rod itself, resulting in part of the focal region being located inside the buffer rather than within the test object. Additionally, when the elements of the PA probe are excited individually, the ultrasonic signals can interfere with each other as they propagate through the buffer rod. The time delays applied to achieve beam steering and focusing cannot be accurately maintained throughout the propagation path. As a result, the intended beamforming effect occurs within the buffer rod rather than in the testing object, significantly reducing inspection effectiveness [62-65].

To solve the problem from the limitations of the bulk buffer rod, a waveguide buffer designed based on the characteristics of guided waves offers a solution. Fukuchi et. al. investigated the characteristics of stacked plate regions for PA probes. The author discusses transverse and longitudinal wave focusing in an elastic medium by controlling the wave field propagating in a stacked thin plate region using the characteristics of Lamb waves in thin plates, shown in Fig. 1.2, which can be theoretically predicted from the dispersion curves [66]. Our idea relating to waveguide buffer is motivated by the problems happened in high temperature non-destructive testing for nuclear powerplants and inspired from the research conducted by Fukuchi et. al. In this thesis, the technique of ultrasonic testing using waveguide will be explained specifically.

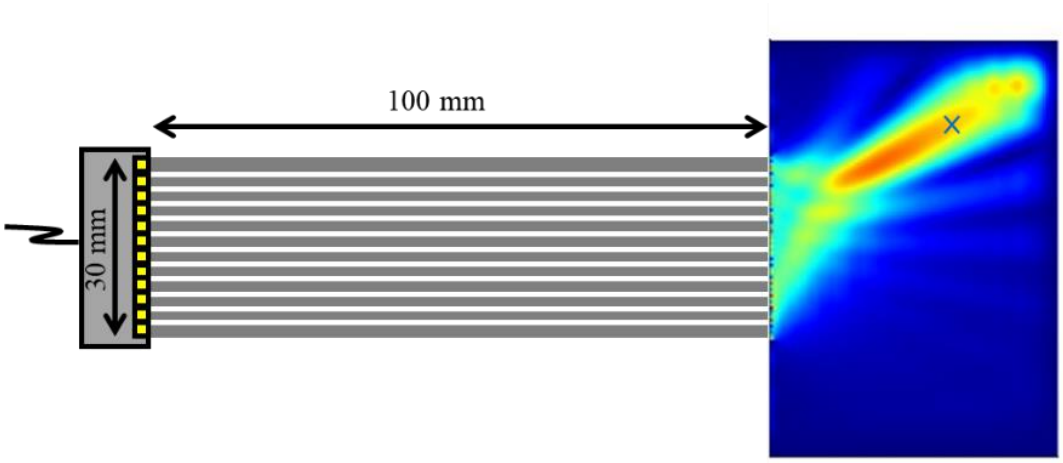

Figure 1.2: Ultrasonic focusing with a stacked plate region [66]

1.2 Outline of the thesis

This thesis can be generally divided into three parts. Chapter 2 describes the theory of wave propagation in several different kinds of conditions and mainly describes the theory of guided waves. Chapter 3 describes the technology of phased array using in non-destructive testing. Chapters 4-6 describes the investigations of phased array imaging with two different waveguide buffers.

Chapter 2 first reviews the background of wave propagations in different conditions including wave propagating in infinite media. Then the guided waves and the properties on thin plate are described, dispersion curve of Lamb wave and wave propagation in circular cylinder will be provided.

Chapter 3 introduces the phased array technology. Information of linear array will be introduced and the two data acquiring and post-processed algorithms, plane wave imaging (PWI) and full matrix capture/total focusing method (FMC/TFM) will be explained.

Chapter 4 introduces numerical calculation research on phased array imaging with a stacked plate buffer. Effective detecting region (EDR) is introduced by theoretical deviations and numerical calculations.

Chapter 5 introduces the experiment investigation on phased array imaging with a stacked plate buffer. The problem of trailing wave happened in the experiments will be investigated theoretically and numerically and then solved by extending the width of the buffer plate.

Chapter 6 introduces the experiment investigation on phased array imaging with

a buffer consisting of a bundle of circular cylinders to solve the problem of trailing wave happened in the experiment introduced in chapter 5.

Chapter 7 summarizes the research introduced in this thesis. Based on the research introduced in this thesis, recommendations for conducting the are also provided.

Chapter 2 Guided waves

2.1 Background

In this thesis, experiments are conducted to investigate the feasibility of phased array imaging with a waveguide buffer. The experiment devices include three parts: a specimen, a waveguide buffer, and a PA probe. For waveguide buffers, two different kinds of waveguide are employed as the waveguide to consist of a buffer, plates and circular cylinders. Thus, in this chapter, the following information relating to this thesis is introduced.

Firstly, this chapter introduces the fundamental concept of ultrasonic waves propagating in infinite media, which relates to the waves propagating in the specimen. In this thesis, the longitudinal wave velocity will be considered for composing the algorithms of the defect imaging.

Secondly, the dispersion properties of guided waves propagating in plate and circular cylinder are introduced. Dispersion occurs when the waves are confined within a structure, and different frequency components or different modes of wave travel at different velocities. Understanding the dispersion curves of different guided waves, which show the relationship between the frequency of the wave, geometry parameter of waveguide and propagating velocity of the wave, is very important. In the research introduced in this thesis, the propagating velocity of guided waves is considered to compose the defect imaging algorithms when the phased array probe is paired with a waveguide buffer.

2.2 Wave equations using potential functions

The theory of wave equations in the infinite media had been well developed in many textbooks [67,68]. This section summarizes the basic information of wave propagation in infinite media.

For isotropic elastic medium, the governing equation can be written as:

$$\mu\boldsymbol{\nabla}^2\boldsymbol{u} + (\lambda+\mu)\boldsymbol{\nabla}\boldsymbol{\nabla}\cdot\boldsymbol{u} = \rho\frac{\partial^2\boldsymbol{u}}{\partial t^2}, \tag{2.1}$$

where $\boldsymbol{u}$ is the particle displacement vector, ρ is the mass density of the material, μ and λ

are the Lame constants. $\boldsymbol{\nabla}^2$ is the Laplacian operator. Based on Helmholtz decomposition, the displacement $\boldsymbol{u}$ can be represented as the sum of the gradient of a compressional scalar potential ϕ and the curl of vector potential $\boldsymbol{H}$:

$$\boldsymbol{u} = \boldsymbol{\nabla}\phi + \boldsymbol{\nabla} \times \boldsymbol{H}, \tag{2.2}$$

where $\boldsymbol{H}$ has zero divergence:

$$\boldsymbol{\nabla} \cdot \boldsymbol{H} = 0. \tag{2.3}$$

The equation of motion Eq. (2.1) can be separated into two independent equations for two potentials:

$$\boldsymbol{\nabla}^2\phi = \frac{1}{c_L^2}\frac{\partial^2\phi}{\partial t^2}, \tag{2.4}$$

$$\boldsymbol{\nabla}^2\boldsymbol{H} = \frac{1}{c_T^2}\frac{\partial^2\boldsymbol{H}}{\partial t^2}, \tag{2.5}$$

where c_L and c_T are the longitudinal wave velocity and transverse wave velocity in infinite isotropic medium and can be expressed as:

$$c_L = \sqrt{\frac{\lambda + 2\mu}{\rho}}, \tag{2.6}$$

$$c_T = \sqrt{\frac{\mu}{\rho}}. \tag{2.7}$$

The general solution for Eqs. (2.4) and (2.5) are

$$\phi = \phi_0 e^{i(kz-\omega t)}, \tag{2.8}$$

$$\boldsymbol{H} = \boldsymbol{H_0} e^{i(kz-\omega t)}, \tag{2.9}$$

where ϕ_0 and $\boldsymbol{H_0}$ is the arbitrary initial constants determined by initial values, k is the wavenumber, ω is angular frequency.

2.3 Guided waves

Guided waves are wave modes whose propagation is constrained by a structural form or boundary, which not only directs the wave but also determines its characteristics.

The propagation behavior depends on the material's density, elastic properties, the boundary conditions as well as geometry of the cross-section.

Guided waves are intrinsic structural phenomena, closely corresponding to the structure's natural vibrational properties. For a finite plate with defined thickness, length, and width, these natural modes, such as bending and in-plane extensional vibrations, can be readily calculated as unforced resonances. However, in an infinite plate, such discrete vibration modes do not exist. Instead, the structure supports guided waves that can propagate indefinitely. These guided wave modes retain characteristics such as bending and extensional motion, like the vibration modes of bounded structures, but are continuous in nature and are described by their specific frequency, velocity, and spatial mode shape. In fact, the vibration modes of a finite structure can be viewed as the result of reverberating guided wave modes between boundaries. Theoretically, both guided waves and natural vibrations are unforced steady-state solutions to the equations of motion, differing only in their boundary conditions.

A key property of guided wave is the ability to propagate over long distances. The waveguide structure confines the energy within boundaries of waveguide, preventing it from spreading as it would in an unbounded medium. For instance, waves along a tensioned wire travel in a single spatial dimension, while waves from a point source in free space radiate in three dimensions, causing a more rapid decrease in amplitude with distance. This is why surface waves from earthquakes, guided along the surface, can be more destructive than body waves reflected from deeper strata: they spread in two dimensions instead of three. This long-range propagation capability makes guided ultrasonic waves attractive for NDT applications.

Another important feature of guided wave is the dispersive nature: the propagation velocity typically changes with frequency. As a result, the waveform of a wave packet changes during propagation. Because such signals contain a finite frequency bandwidth, and the constituent frequency components travel at different speeds, the wave packet spreads over time and its amplitude diminishes. This dispersion is not due to the material properties but rather arises from the boundary conditions imposed by the waveguide geometry [69].

In this thesis, plate and circular cylinder will be used to consist of two different types of waveguide buffer. When considering the wave propagation inside these waveguides, dispersion curve, which reveals the wave propagation velocity, frequency and geometry parameters of the waveguide, is very important. However, for the dispersion curve of Lamb wave propagating in plate and the dispersion curve of waves propagating in a circular cylinder, the analytical solution cannot be obtained. Thus, in

calculating the dispersion curve, the numerical solution is always used to compose the dispersion curve. In this thesis, the dispersion curve of Lamb wave and wave propagation in circular cylinder will be calculated by semi-analytical finite element (SAFE) method.

2.3.1 Guided wave propagation in a plate

In chapter 4 and chapter 5 in this thesis, plate structure performs as a kind of waveguide to transmit the signals from phased array probe. Thus, the properties of Lamb wave propagation in a plate will be investigated.

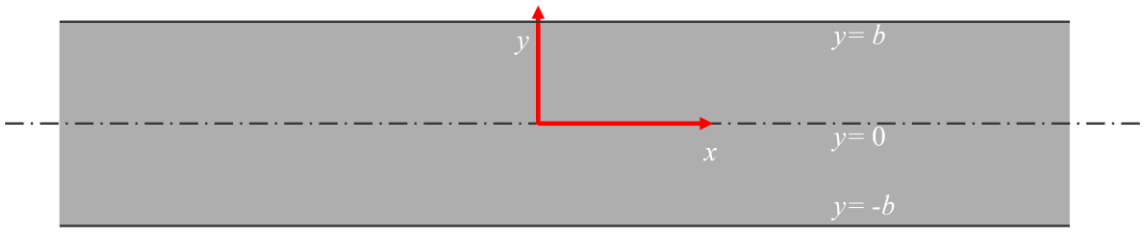

Figure 2.1. The geometry of cross-section of plate for explaining the Lamb wave

Now we consider plate geometry in Fig. 2.1. Assuming the thickness of the plate is $2b$ and the x-axis is overlapped with the centerline of the plate. As plane strain condition hold in the z direction, we have that:

$$u_x = \frac{\partial \phi}{\partial x} + \frac{\partial H_z}{\partial y}, \tag{2.10}$$

$$u_y = \frac{\partial \phi}{\partial y} - \frac{\partial H_z}{\partial x}. \tag{2.11}$$

where u_x is the displacement in x-direction and u_y is the displacement in y-direction. Then we have:

$$\boldsymbol{\nabla}^2 \phi = \frac{1}{c_L^2} \frac{\partial^2 \phi}{\partial t^2}, \tag{2.12}$$

$$\boldsymbol{\nabla}^2 H_z = \frac{1}{c_T^2} \frac{\partial^2 H_z}{\partial t^2}, \tag{2.13}$$

The boundary conditions considered here are expressed by:

$$\tau_{yy} = \tau_{xy} = \tau_{zy} = 0, \quad \text{when } y = \pm b, \tag{2.14}$$

where τ_{yy} is the normal stress in the *y*-direction on a surface normal to *y*-direction, τ_{xy} is the shear stress in the *y* direction on a surface normal to *x*-direction, τ_{zy} is the shear stress in the *y* direction on a surface normal to *z*-direction. For symmetric mode, the equation is written as:

$$\frac{\tan\beta b}{\tan\alpha b} = -\frac{4\alpha\beta k^2}{(k^2-\beta^2)^2}, \tag{2.15}$$

where *k* is the wavenumber. For antisymmetric mode, the equation is written as:

$$\frac{\tan\beta b}{\tan\alpha b} = -\frac{(k^2-\beta^2)^2}{4\alpha\beta k^2}. \tag{2.16}$$

For α and β, these two variables can be expressed as:

$$\alpha^2 = \frac{\omega^2}{c_L^2} - k^2, \qquad \beta^2 = \frac{\omega^2}{c_T^2} - k^2. \tag{2.17}$$

The frequency equations of Lamb wave, Eqs. (2.16) and (2.17), are nonlinear functions which can be written as the form of:

$$f(k,\omega) = 0, \tag{2.18}$$

and the relationship among wavenumber k, angular frequency ω, and phase velocity, c_p, can be expressed as:

$$c_p = \frac{\omega}{k}. \tag{2.19}$$

In this way, each value of k can find a value of ω by the Eqs. (2.15)-(2.17), then the relationship between the phase velocity c_p and product of frequency and thickness fd of the plate can be determined.

When the $fd \to 0$, the relation between the phase velocity of A0 mode Lamb wave and fd is [68, 70]:

$$\begin{aligned} C_{pA0} &\to \pi^{\frac{1}{2}}\left\{\frac{E}{3\rho(1-\nu^2)}\right\}^{\frac{1}{4}}(fd)^{\frac{1}{2}} \\ &= (2\pi c_T)^{\frac{1}{2}}\left[\frac{1}{3}\left\{1-\left(\frac{c_T}{c_L}\right)^2\right\}\right]^{\frac{1}{4}}(fd)^{\frac{1}{2}}, \end{aligned} \tag{2.20}$$

where *E* is Young's module and ρ is density of the material, ν is the Poisson's ratio. Then for S0 mode Lamb, the phase velocity will converge to a certain value called c_{plate}.

$$C_{pS0} \to \sqrt{\frac{E}{\rho(1-\nu^2)}} = 2c_T\sqrt{1-\left(\frac{c_T}{c_L}\right)^2} \equiv c_{plate}\,. \tag{2.21}$$

The phase velocity dispersion curve of Lamb wave is shown in Fig. 2.2.

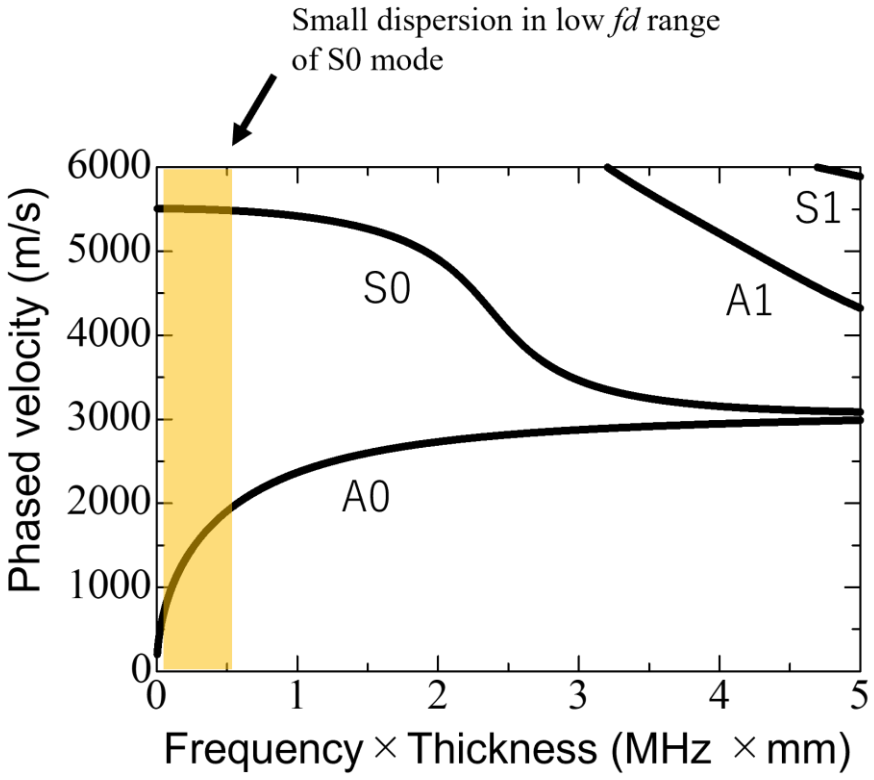

Figure 2.2. Phase velocity dispersion curve of Lamb wave

For group velocity dispersion curve, it can be obtained from the equation

$$c_g = \frac{d\omega}{dk}. \tag{2.22}$$

Then, the group velocity dispersion curve can be also obtained, which is shown in Fig. 2.3.

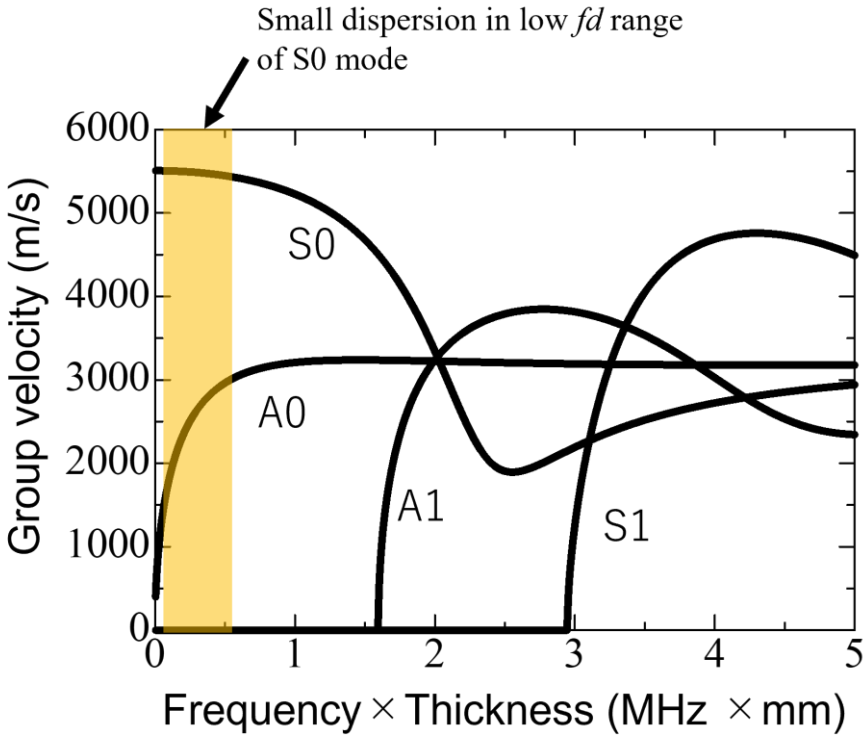

Figure 2.3. Group velocity dispersion curve of Lamb wave

In the dispersion curves of Lamb wave shown in Fig. 2.3 and Fig. 2.4, the yellow areas are the low frequency range of the dispersion curves. In this thesis, the S0 mode Lamb wave in low fd range will be considered due to following reasons.

Firstly, in the low fd range, the dispersion nature of S0 mode Lamb wave is relatively small. In this condition, when the Lamb waves propagate in the plate of stacked plate buffer, the distortion of the wave is relatively small, so the imaging can be relatively clear.

Secondly, the influence from other modes, such as A0, S1 and A1 can be smaller. In the low fd range, the difference between propagating velocity of A0 and S0 mode Lamb wave is very large and there are no S1 or A1 mode waves. Thus, the noise will be smaller and the imaging quality can be ensured.

2.3.2 Guided wave propagation in a circular cylinder

In chapter 6 in this thesis, circular cylinder performs as a kind of waveguide to transmit the signals from phased array probe. Thus, the properties of guided wave

propagation in a circular cylinder need to be investigated.

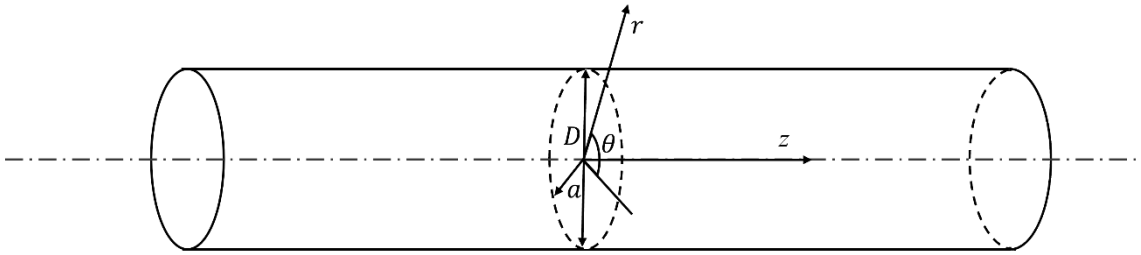

Figure 2.4. The plate geometry for explaining the guided wave propagation in a circular cylinder.

Now we consider circular cylinder in Fig. 2.4. Assuming the radius of the circular cylinder is *a,* diameter of the cylinder is *D*, in the cylindrical coordinate system, we have:

$$u_r = \frac{\partial \phi}{\partial r} + \frac{1}{r}\frac{\partial H_z}{\partial \theta} - \frac{\partial H_\theta}{\partial z}, \tag{2.23}$$

$$u_\theta = \frac{1}{r}\frac{\partial \phi}{\partial r} + \frac{\partial H_r}{\partial z} - \frac{\partial H_z}{\partial r}, \tag{2.24}$$

$$u_z = \frac{\partial \phi}{\partial z} + \frac{1}{r}\frac{\partial r H_\theta}{\partial \theta} - \frac{\partial H_\theta}{\partial z}, \tag{2.25}$$

$$\boldsymbol{\nabla}^2 \phi = \frac{1}{c_L^2}\frac{\partial^2 \phi}{\partial t^2}, \tag{2.26}$$

$$\boldsymbol{\nabla}^2 \boldsymbol{H} = \frac{1}{c_T^2}\frac{\partial^2 \boldsymbol{H}}{\partial t^2}, \tag{2.27}$$

where r, θ and z are the coordinates in cylindrical coordinate system, r is the distance from the z-axis, which is the centerline of the cylinder, θ is the rotation angle around the z-axis and z is position along the z-axis. The H_z represents the shear wave motion along the axis of the cylinder, H_θ represents circumferential shear motion and H_r represents the shear wave motion perpendicular to the cylinder surface. The u_r, u_θ, u_z are radial displacement, circumferential displacement and axial displacement, respectively, and the Laplacian operator for the cylindrical coordinate system can be expressed as:

$$\boldsymbol{\nabla}^2 = \frac{\partial^2}{\partial r^2} + \frac{1}{r}\frac{\partial}{\partial r} + \frac{1}{r^2}\frac{\partial^2}{\partial \theta^2} + \frac{\partial^2}{\partial z^2}, \tag{2.28}$$

The boundary conditions considered here are expressed by:

$$\tau_{rr} = \tau_{rz} = \tau_{r\theta} = 0, \text{ when } r = a, \tag{2.29}$$

where τ_{rr} is the radial normal stress on a surface normal to the radial direction, τ_{rz} is the axial shear stress on a surface normal to the radial direction, $\tau_{r\theta}$ is the circumferential shear stress on surface normal to the radial direction. The frequency equation only for longitudinal modes is written as:

$$\begin{aligned}\frac{2\alpha}{a}\left(\beta^2 + k^2\right)J_1(\alpha a)J_1(\beta a) - \left(\beta^2 - k^2\right)^2 J_0(\alpha a)J_1(\beta a) \\ - 4k^2\alpha\beta J_1(\alpha a)J_0(\beta a) = 0,\end{aligned} \tag{2.30}$$

where k is the wavenumber of the wave propagating in the z direction, and the J_0 and J_1 in Eq. (2.30) are the zero-order and first-order Bessel functions, respectively. α and β are written as:

$$\alpha^2 = \frac{\omega^2}{c_L^2} - k^2, \beta^2 = \frac{\omega^2}{c_T^2} - k^2. \tag{2.31}$$

Although the dispersion relations of longitudinal modes in a circular cylinder are obtained by solving the nonlinear equation, Eq. (2.30), solving all the modes are intractable due to the complexity of wave propagation in circular cylinder. Therefore, numerical and semi-analytical approaches have become essential tools for analyzing guided wave behavior in a circular cylinder. In this thesis, the semi-analytical finite element (SAFE) method is employed to compute the dispersion curves of guided waves in circular cylinder. The SAFE method is introduced in the next section and then provides the dispersion curves of wave propagation in circular cylinder calculated by SAFE method.

2.3.3 Semi-analytical finite element (SAFE) method

The SAFE method is a useful numerical technique developed for the efficient simulation of wave propagation in structures that exhibit geometric invariance along one direction, such as plates, rods, and pipes. In contrast to full three-dimensional finite element simulations, which discretize the entire volume of the structure and are computationally expensive, the SAFE method takes advantage of the uniformity along the propagation axis to simplify the problem. Specifically, the SAFE approach discretizes

only the cross-sectional area of the structure using conventional finite elements, while treating the wave propagation along the longitudinal axis analytically by assuming harmonic wave solutions.

The displacement field in the SAFE formulation is expressed as a product of a numerically computed cross-sectional mode shape and a harmonic function in the propagation direction. This transforms the original wave equation into a frequency-dependent eigenvalue problem, where the eigenvalues correspond to wavenumbers and the eigenvectors represent displacement mode shapes. Solving this eigenproblem yields dispersion curves for different wave modes, including phase and group velocities, across a wide frequency range.

The SAFE method is particularly for analyzing guided wave behavior in complex or layered media, including those with anisotropic or viscoelastic properties. It provides high accuracy and excellent computational efficiency, making it ideal for applications such as ultrasonic guided wave inspection, structural health monitoring, and transducer design. In these contexts, the SAFE method helps engineers and researchers predict how different wave modes propagate, interact with defects, or respond to varying boundary conditions, all of which are critical for the development of effective nondestructive testing techniques [71].

Fig. 2.5 and Fig. 2.6 show the phase velocity and group velocity dispersion curves of wave propagating in longitudinal direction of a circular cylinder calculated by SAFE, respectively.

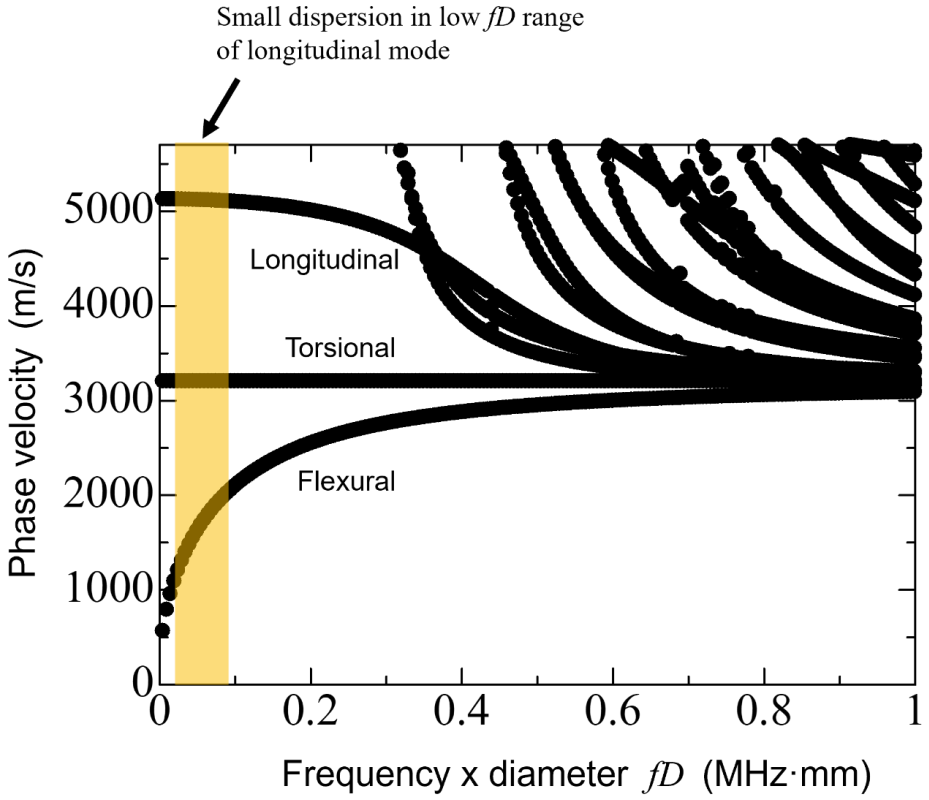

Figure 2.5. Phase velocity dispersion curves of guided wave propagating in a circular cylinder

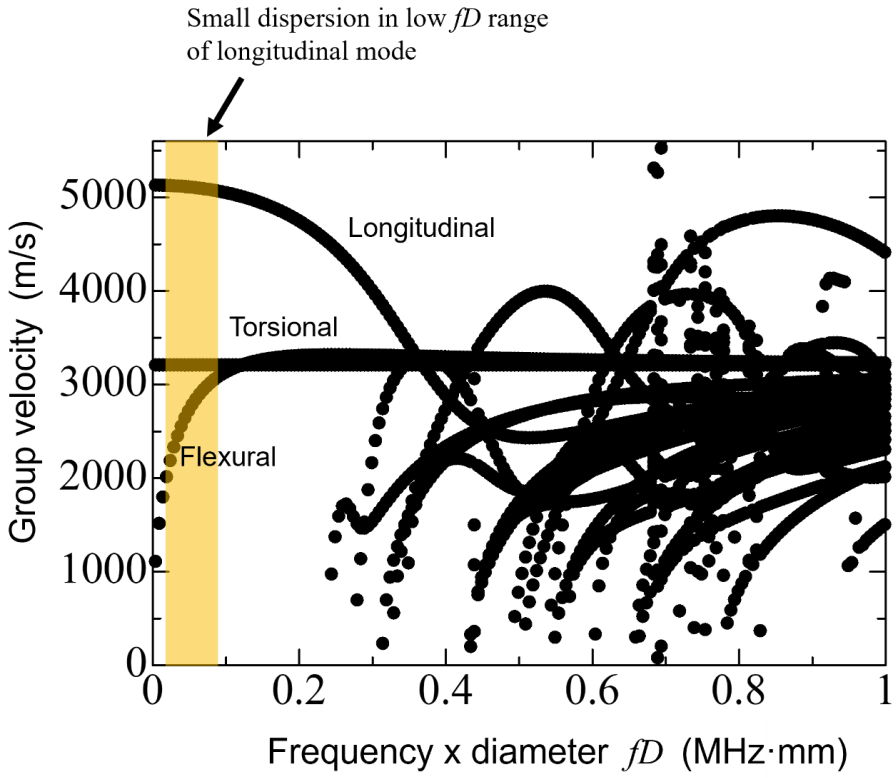

Figure 2.6. Group velocity dispersion curves of guided wave propagating in a circular cylinder

From the dispersion curves, three modes of waves can be observed, longitudinal mode wave, torsional mode wave and flexural mode wave. In the low fD range, which is marked by the yellow area, fundamental modes of longitudinal, torsional and flexural cylinder wave can be observed. In the yellow area, the flexural mode wave is with very significant dispersion phenomena but with relatively low group velocity. The torsional wave is without dispersion phenomena but still very low group velocity comparing to the longitudinal mode wave. Similar to plate waveguide when utilizing the property of S0 mode Lamb wave, circular cylinder can be used as a waveguide to consists of a waveguide buffer when utilizing the propagating property of first longitudinal mode wave in low fD range.

Chapter 3 Ultrasonic phased array imaging

3.1 Introduction

Phased array (PA) technology has experienced continuous evolution since its conceptual origin in the early 20th century. Initially a theoretical idea, it became practically viable during World War II, when the U.S. Lincoln Laboratory demonstrated directional control of wave propagation by mechanically adjusting the positions of array elements. Over the past eight decades, phased array radar has advanced through three significant phases: passive, active, and digital.

To address growing air defense demands during World War II, the United Kingdom established its first coastal radio detection station in 1937. Later, in the 1960s, the U.S. Advanced Research Projects Agency (ARPA) launched the first formal development program for passive phased array radar, incorporating electronically steered and computer-controlled dual-position systems. The intensifying Cold War further heightened the demand for more powerful radar capabilities, spurring rapid technological progress.

In response, the Defense Advanced Research Projects Agency (DARPA) initiated research into microwave and millimeter-wave monolithic integrated circuit (MMIC) technologies. These initiatives produced key advancements, including gallium arsenide (GaAs) circuits, multi-chip integration, precision computer control systems, and sophisticated circuit modeling techniques. The transition to simulation-driven design significantly reduced development cycles compared to conventional modeling approaches.

Beginning in the 1990s, active phased array radar systems were used in new generation military platforms, offering enhanced performance, beam agility, and energy efficiency. Continued operational demands in the following decades have driven further refinement and expansion of PA radar capabilities, solidifying the technology's role in modern defense infrastructure [72-74].

In UT, sensitivity largely depends on the amount of ultrasonic energy reflected from defects. One straightforward way to increase the reflected energy is to raise the transmitted energy. However, this approach typically also amplifies background noise. An alternative method is to focus the ultrasonic beam onto the flaw. In this case, the beam intensity at the defect location is increased, enhancing the reflected signal without raising

the overall transmission power. At the same time, noise signals from unfocused regions are reduced, thereby improving the signal-to-noise ratio and detection sensitivity.

Phased array technology allows ultrasonic beams to be electronically focused at specific locations without mechanical movement. Phased array transducers can be configured in various geometries, including linear, square, circular, angular, and convex arrangements. In the simulations and experimental work presented in this thesis, a linear phased array transducer is employed. Therefore, the following discussion will specifically focus on the characteristics and application of the linear configuration [42-47].

In this chapter, the principle of the linear phased array technology used in this thesis will be introduced. The structure of the linear array used in this thesis will be introduced. Then two imaging algorithms used in this thesis will be introduced in detail.

3.2 Linear array

Linear PA probe has elements arranged in a straight line and are widely used in PAUT. The structure and the parameters of the ultrasonic linear array will be introduced [75].

Linear array has parameters such as pitch p, which is the inter-element spacing, and the element number N. Fig. 3.1 shows the schematic when a PA probe directly contacts a specimen. The contact surface of phased array probe and specimen is set to be $y = 0$ and the arrangement direction of the PA elements is set to be x-direction. The grey area is the test specimen, the yellow squares are the elements of PA probe, the red circle is the origin (0,0) of the imaging area. The grid within the test specimen indicates the range of imaging area calculation point of intensity. The horizontal rightward direction is the positive x-axis, and the vertical downward direction is the positive y-axis. As shown in the Fig. 3.1, the center of the x-direction of the PA probe and the position of the contact point with the test specimen are set as the origin (0,0). X_R and Y_R are the dimension of the range of imaging area.

The position of the number i element $\mathbf{r}_i$ and the coordinate of the point $\mathbf{x}$ (x,y) in the imaging area can be defined as:

$$\mathbf{r}_i = \left[-\frac{p(N-1)}{2} + p(i-1), 0 \right], \tag{3.1}$$

where $i = 1,2,3 \ldots N$,

$$\mathbf{x}(x,y) = \left[-\frac{X_R}{2} + \frac{X_R}{2N_x} + \frac{X_R}{N_x}(m-1), \frac{Y_R}{2N_y} + \frac{Y_R}{N_y}(n-1) \right], \tag{3.2}$$

where $m = 1,2,3 \ldots N_x$ and $n = 1,2,3 \ldots N_y$.

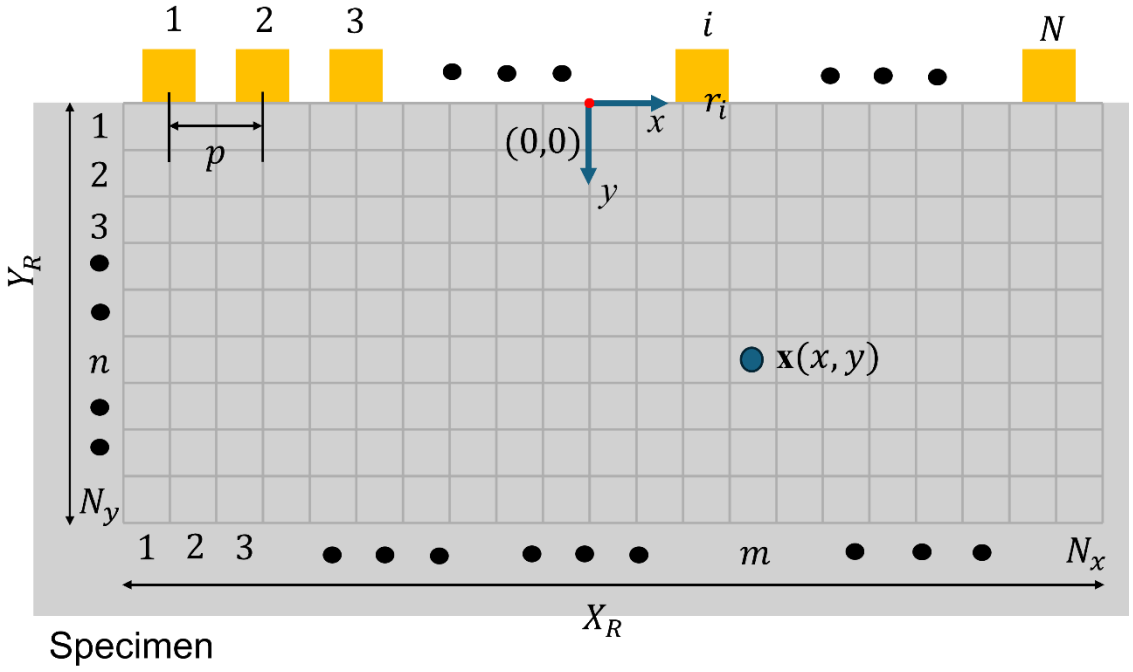

Figure 3.1: Schematic diagrams of a phased array probe contacting with a specimen.

3.3 Imaging algorithms

3.3.1 Introduction

Phased array imaging algorithms including such as full matrix capture/total focusing method (FMC/TFM), plane wave imaging (PWI), sector scan. In this thesis, according to the algorithms used in the experiments and numerical calculations, the principles of FMC/TFM and PWI [76] will be introduced in the following content. In case of linear array and our experiments and simulations are all conducted in 2D cases, the algorithm will be introduced for 2D problems.

3.3.2 Plane wave imaging

When applying PWI in defect imaging, a planar wavefront is generated by exciting elements of PA probe simultaneously, and the echoes from the object to be tested are acquired simultaneously by each element to reconstruct an image in post-processing. Different to conventional ultrasonic imaging, the frame rate is limited by the time of round-trip for wave from probe to defect. Thus, it is easier to get a high frame rate in PWI.

When applying PWI without a buffer, shown in Fig. 3.2, assuming the waves are propagating in *x*-*y* plane, a linear phased array is attached with the upper end of the specimen. The time of element $\mathbf{r}_i$ receive the echo from the position $\mathbf{x}$ (*x*,*y*), t_i, can be expressed as:

$$t_i = \frac{y + |\mathbf{x} - \mathbf{r}_i|}{c}. \tag{3.3}$$

If the time width of the incident wave is τ_0, the waveform extracted from the reflected wave received from the position $\mathbf{x}$, u_i, from time point t_i to $t_i + \tau_0$ is given by:

$$v_i(\mathbf{x}, t) = u_i(t + t_i) \quad \text{for } 0 < t_i < \tau_0. \tag{3.4}$$

Then obtain v_i from the reflected waveforms received by each element and then sum of all the v_i,

$$U(\mathbf{x}, t) = \sum_{i=1}^{N} v_i(\mathbf{x}, t). \tag{3.5}$$

Then find the integration of square of $U(\mathbf{x}, t)$ in the time period from 0 to τ_0, the intensity of the reflected wave at position $\mathbf{x}$ can be determined as:

$$I(\mathbf{x}) = \frac{1}{\tau_0} \int_0^{\tau_0} \{U(\mathbf{x}, t)\}^2 \, dt. \tag{3.6}$$

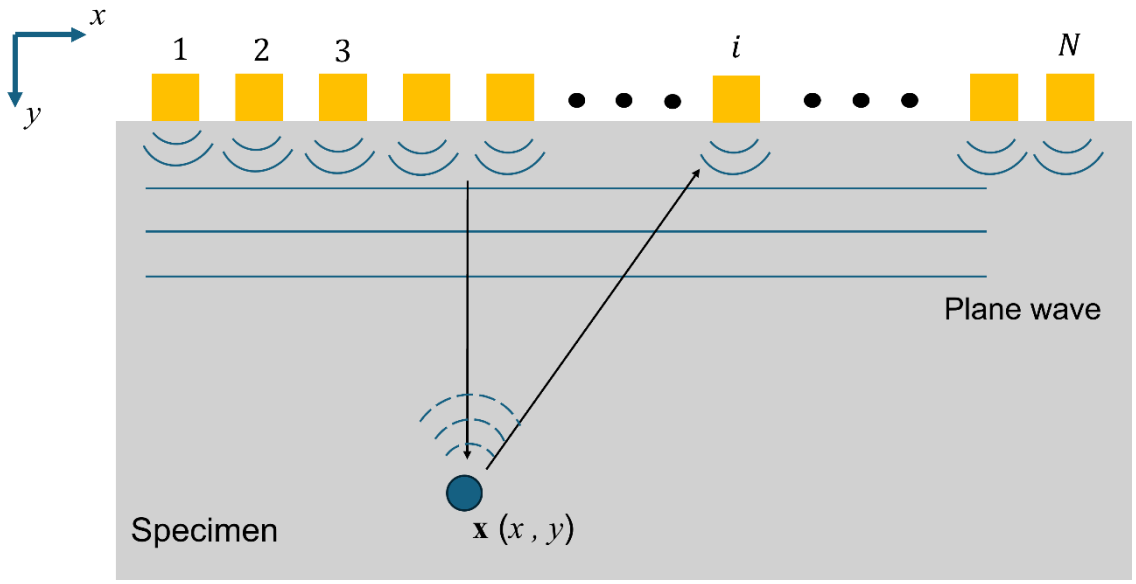

Figure 3.2: Schematic diagrams for showing concept of PWI when without a buffer

When applying PWI with a buffer, as shown in Fig. 3.3, the blue area is the waveguide buffer which connects the PA elements and the specimen. Assuming the length of the buffer is L, the velocity of the wave propagate in buffer is c_b, then the round trip inside the buffer of wave propagating in buffer, t_b, is:

$$t_b = \frac{2L}{c_b}. \tag{3.7}$$

Then Eq. (3.3) becomes:

$$t_i = \frac{y + |\mathbf{x} - \mathbf{r}_i|}{c} + t_b. \tag{3.8}$$

Then following the Eqs. (3.4)-(3.6) to calculate the $I(\mathbf{x})$.

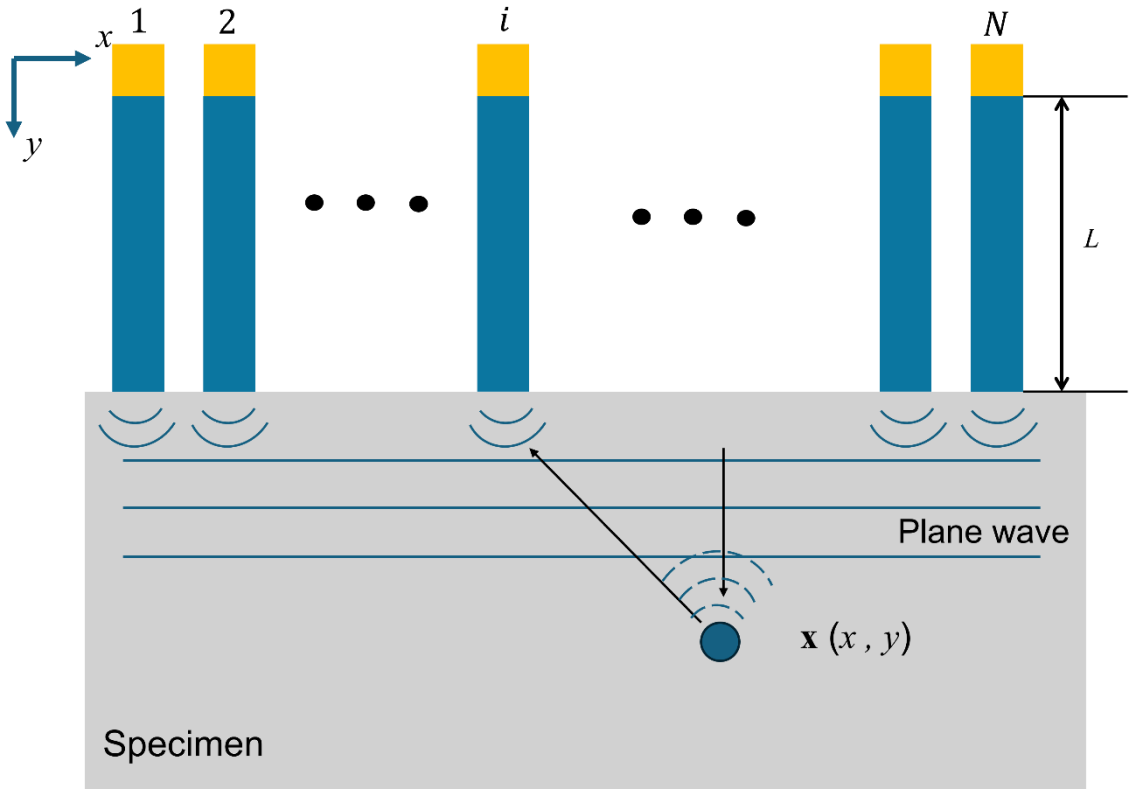

Figure 3.3: Schematic diagrams for showing concept of PWI when with a buffer

3.3.3 Full matrix capture/total focusing method

The FMC/TFM method involves transmitting signals with each element of the probe one by one and receiving at all the elements for each shot. A set of $N \times N$ signals is therefore collected.

When applying FMC/TFM without a buffer, shown in Fig. 3.4, assuming the waves are propagating in *x*-*y* plane, a linear phased array is attached with the upper end of the specimen. The time of element $\mathbf{r}_i$ receive the echo emitted by element $\mathbf{r}_j$ and reflected from the position $\mathbf{x}$ (x,y), t_{ij}, can be expressed as

$$t_{ij} = \frac{|\mathbf{x} - \mathbf{r}_i| + |\mathbf{x} - \mathbf{r}_j|}{c}. \tag{3.9}$$

If the time width of the incident wave is τ_0, the waveform extracted from the reflected wave received from the position $\mathbf{x}$, u_{ij}, from time point t_{ij} to $t_{ij} + \tau_0$ is given by:

$$v_{ij}(\mathbf{x}, t) = u_{ij}(t + t_{ij}) \quad \text{for } 0 < t_{ij} < \tau_0. \tag{3.10}$$

Then obtain v_{ij} from the reflected waveforms received by each element and then sum of

all the v_{ij},

$$U(\mathbf{x},t) = \sum_{j=1}^{N}\sum_{i=1}^{N} v_{ij}(\mathbf{x},t)\,. \tag{3.11}$$

Then find the integration of square of $U(\mathbf{x},t)$, the intensity of the reflected wave at position **x** can be determined as

$$I(\mathbf{x}) = \frac{1}{\tau_0}\int_0^{\tau_0} \{U(\mathbf{x},t)\}^2\ dt\,. \tag{3.12}$$

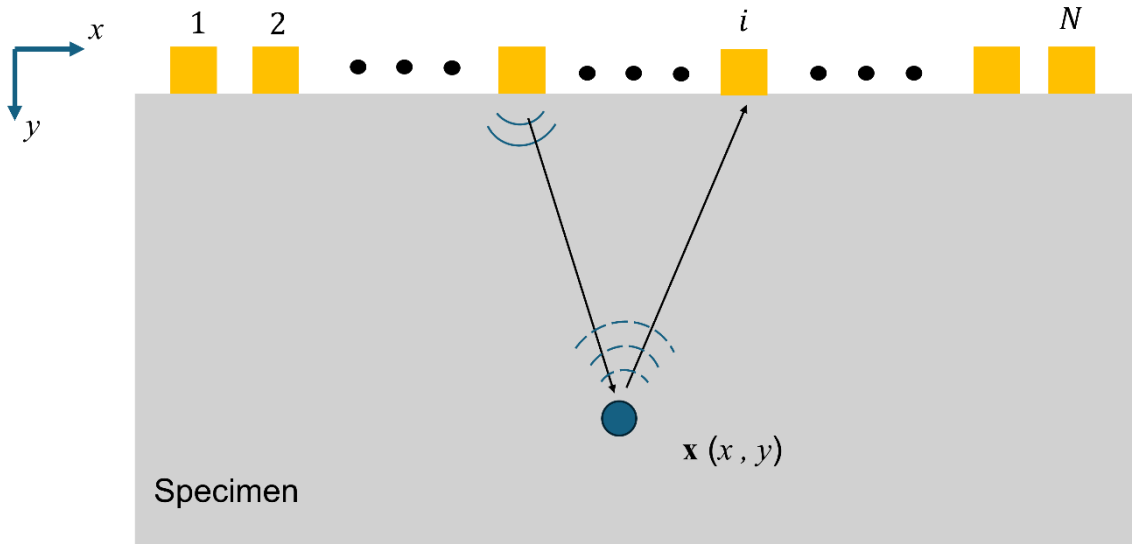

Figure 3.4: Schematic diagrams for showing concept of FMC/TFM when without a buffer

When applying FMC/TFM with a buffer, as shown in Fig. 3.5, the blue area is the waveguide buffer which connects the PA elements and the specimen. Assuming the length of the buffer is L, the velocity of the wave propagate in buffer is c_b, then the round trip inside the buffer of wave propagate in buffer, t_b, is:

$$t_b = \frac{2L}{c_b}. \tag{3.13}$$

Then Eq. (3.3) becomes:

$$t_{ij} = \frac{|\mathbf{x}-\mathbf{r}_i| + |\mathbf{x}-\mathbf{r}_j|}{c} + t_b. \tag{3.14}$$

Then following the Eqs. (3.10)-(3.12) to calculate the $I(\mathbf{x})$.

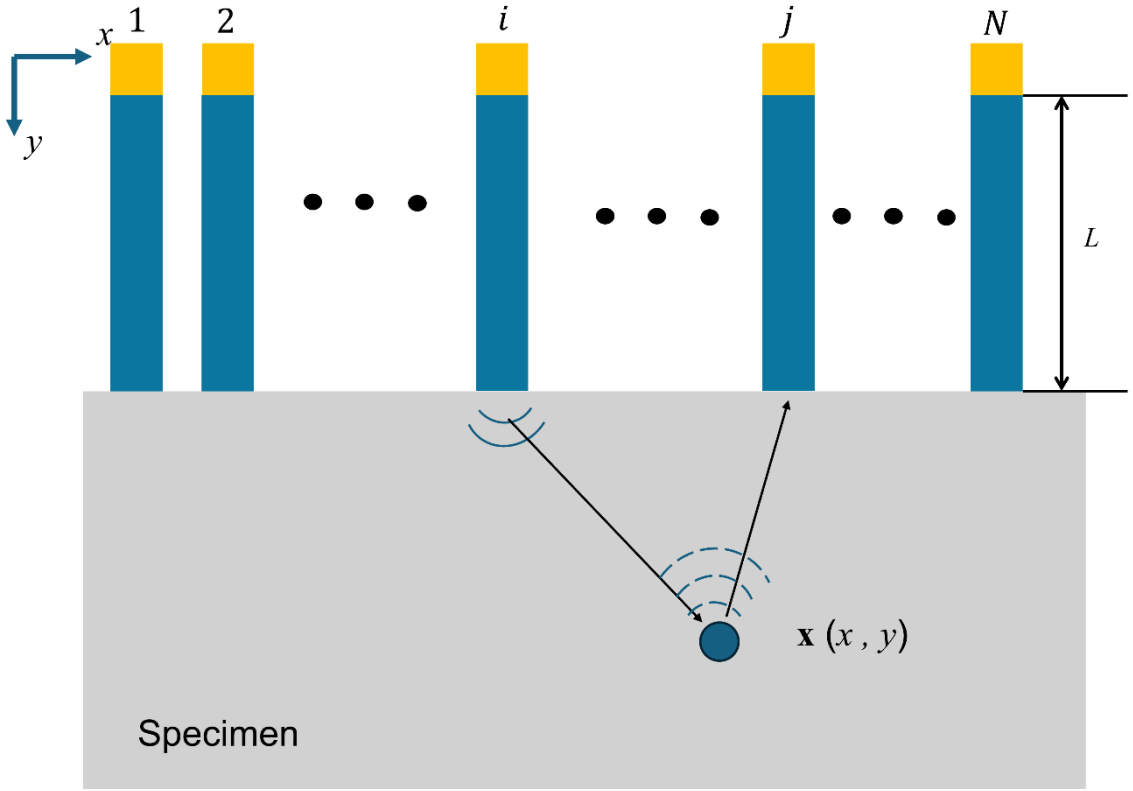

Figure 3.5: Schematic diagrams for showing concept of FMC/TFM when with a buffer

Chapter 4 Numerical analysis of phased array imaging with stacked plate buffer

4.1 Idea of the waveguide buffer

In the following three chapters, the validation of phased array imaging with waveguided buffers will be presented. Numerical calculations and experiments will be applied to the following studies.

As introduced in chapter 1, when the PA probe is trying to test the high temperature object, the probe will be destroyed by direct contact. Thus, a bulk buffer rod can be a solution to connect the PA probe with a high temperature object. Because of near field limit as mentioned in chapter 3, when using the conventional bulk buffer rod and phased-array probe, the distance between the incident position and the focal point may be too long to focus which can be focused when without a bulk buffer rod. The performance of the PA probe will be undermined in this condition. Thus, to use the buffer to protect the PA probe from high temperature while transmitting the signals to the specimen, an alternative method is needed for designing the structure of the buffer.

The idea of the waveguided buffer is from the research of ultrasonic focusing with a stacked plate region conducted by Fukuchi et al. which proposed two ultrasonic focusing techniques using stacked thin plate region. The focusing performance achieved with the proposed region was comparable to that obtained without a buffer using the phased array transducer. In addition, the stacked thin plate region enabled focusing at distances that were unachievable with conventional buffer rods. Thus, the stacked thin plate region holds promise for applications where direct attachment of phased array probes is difficult, such as the non-destructive testing of high temperature objects [66].

4.2 Theory of phased array imaging with a stacked plate buffer

To explain the function of the stacked plate buffer, it is necessary to understand the nature and propagation characteristics of Lamb wave propagating in a plate. Because the dispersion curve shows the relation between wave velocity and product of frequency and plate thickness, dispersion curve is very necessary to select proper parameters of the plates and the PA probe.

In the numerical calculations shown in chapter 4, material of all the components of the calculation model is set to be aluminum alloy, which has longitudinal and transverse wave velocities of 6400 m/s and 3170 m/s, respectively. The dispersion curve of aluminum alloy is shown in Fig. 4.1. The horizontal axis represents the product of the frequency (f) and the thickness of the plate (d) while the vertical axis represents the wave velocity.

Shown in Fig. 4.1, in low frequency range around fd = 1MHz mm, the slope of the line is relatively small than high frequency region. Thus, in the low fd range, dispersion nature of the S0 mode is relatively small, which can have the effect that ultrasonic pulse signal can maintain the original waveform in transmitting in a plate. The S0 mode in the low fd range has a longitudinal vibration parallel to the longitudinal axis direction, while the A0 mode has a bending vibration in the vertical direction. This indicates that only the S0 mode is efficiently excited when a phased array probe, which excites longitudinal waves from each element, is in contact with the plate end.

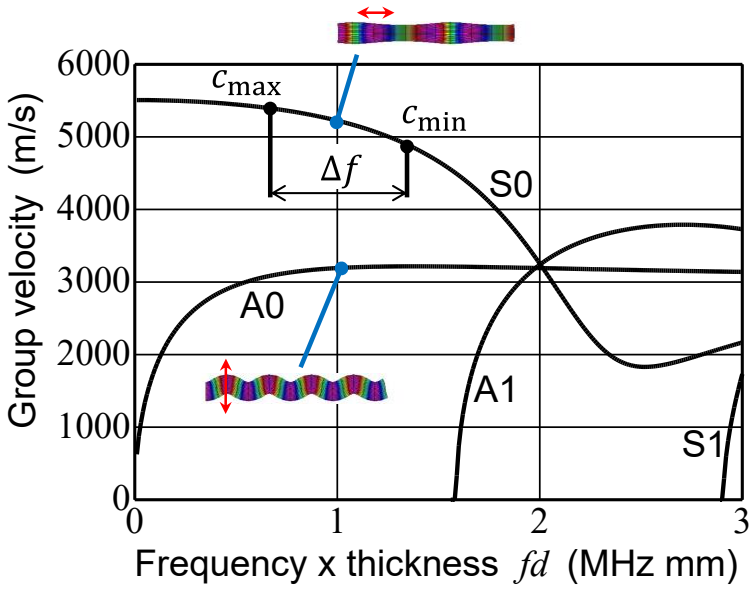

Figure 4.1: Group velocity dispersion curve of Lamb wave in the low fd range.

4.3 Finite element simulation

To investigate the performance of the stacked plate buffer, finite element simulations have been used to investigate the wave propagation in the buffer and specimen. The calculations of two-dimensional wave propagation were conducted under

the conditions of plane strain with COMSOL Multiphysics® by Finite Element Method (FEM).

Finite element method (FEM) is a widely used numerical technique for solving complex problems governed by partial differential equation (PDE), especially in engineering and applied physics. It provides an approximate solution by dividing a physical domain into a finite number of smaller subdomains called elements, which are interconnected at nodes. Within each element, the solution is approximated using interpolation functions, which represent the variation of the field variable across the element.

FEM is highly versatile and applicable to a wide range of problems, including structural analysis, heat transfer, fluid flow, acoustic propagation, and electromagnetic fields. Its major strength lies in its ability to model arbitrary geometries, heterogeneous material properties, and complex boundary conditions with high accuracy. Due to its generality and robustness, FEM has become a fundamental tool in both academic research and industrial applications, enabling simulation-driven design and analysis across numerous disciplines.

4.3.1 Modelling

Fig. 4.2 shows the calculation model used in the numerical calculation, which assumes that the stacked plate buffer is attached to the phased array probe with 16 elements of 1 MHz center frequency and contacts with a specimen at the other end of the plate. In the setting of modelling, the longitudinal force from the phased array probe is applied at each end of plate to excite the incident wave into each end of plate of the stacked plate buffer.

The plates of the stacked plate buffer are with the identical thickness of 0.9 mm are lined up and are assumed to be perfectly contacting with the vibration elements of PA probe. Each plate is aligned with each PA element without any gap in the joints. The width of each channel is set to be 0.9 mm, which is the same as the thickness of each buffer plate, and the gap between the elements is 0.1 mm. For all the plates in the stacked plate buffer, the left and right surfaces are set to be traction free boundary conditions, which can be expressed as:

$$\tau_{xx} = \tau_{yx} = 0. \tag{4.1}$$

where τ_{xx} is the normal stress in the x-direction on a surface normal to x-direction, τ_{yx} is the shear stress in the y direction on a surface normal to x-direction.

From the phased array probe, vertical dynamic normal force, whose vibration function follows a product of a Gaussian function and a sine function with frequency of 1MHz, is applied to the upper end of each plate and the S0 mode of Lamb wave propagating through the stacked plate buffer is transmitted into the specimen. The specimen is assumed to be perfectly contacted with the lower end of the buffer.

The imaging area is a 60 mm × 40 mm rectangular area and surrounded by absorption region. The absorption region is attached to the left, right and lower edge of the specimen and can absorb all the waves pass through the boundaries of the specimen and absorption region. In this way, the specimen can be assumed to be large enough and the influence from the boundaries of the specimen can be neglected.

The whole geometry is meshed by both triangular elements and rectangular elements. For the area of stacked plate buffer, the meshed elements are rectangular while for specimen the elements are triangular. For observing the wave diffraction near the defects, the mesh element sizes are relatively small. For elements far from the boundary of the defects, including the absorption region, the element sizes are relatively large to decrease the time consumed for calculation.

Two circular hole defects with 3 mm diameter are on the specimen in the first calculation. The center of the bottom of the stacked plate region is defined as the origin of the *xy* coordinates, and the positions of the defects are expressed as (*x, y*). The positions of Defect 1 and Defect 2 are (−10 mm, 20 mm) and (5 mm, 30 mm), respectively.

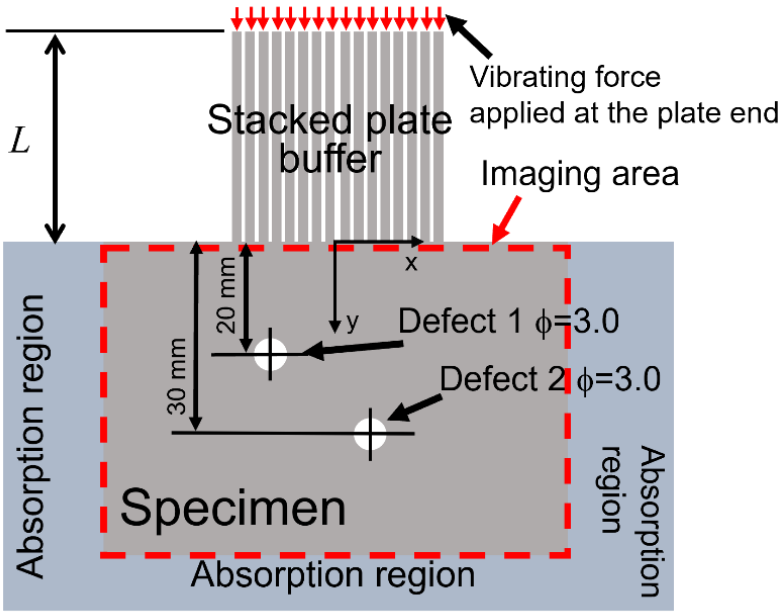

Figure 4.2: Schematic of the two-dimensional calculation model

4.3.2 First calculations

The defect imaging using the PWI without buffer, in other words, L = 0 mm, were first obtained as shown in the imaging result Fig. 4.3 (a). Then, for comparing with the results when using a stacked plate buffer. The imaging using PWI with a buffer of L = 25 mm was obtained as shown in Fig. 4.3 (b). The colors of the images represent intensities calculated by the PWI, normalized by the maximum intensity of each figure. The two defects inside the specimen can be clearly shown in the imaging area at the correct position as shown in Fig. 4.2. However, when the stacked plate buffer of L = 25 mm is used to connect the transducer and the specimen, the reflection from Defect 2 is distorted and can only be less clearly shown in the image. In this condition, the phased array probe cannot perform as well as it directly attached to the specimen. In addition, distinct spurious image behind the defect images were also obtained.

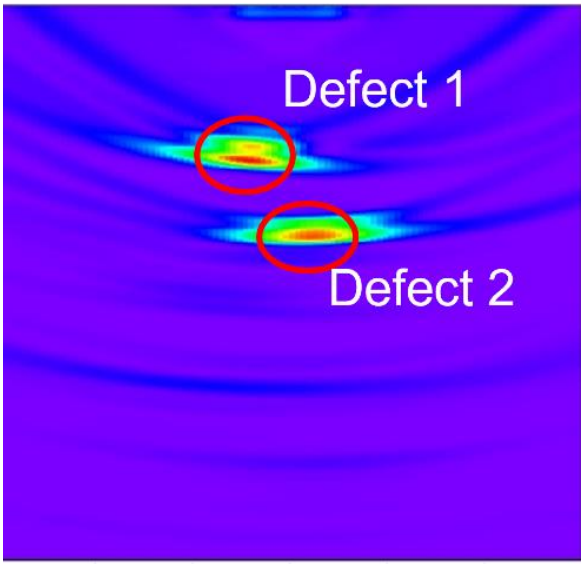

(a) No buffer

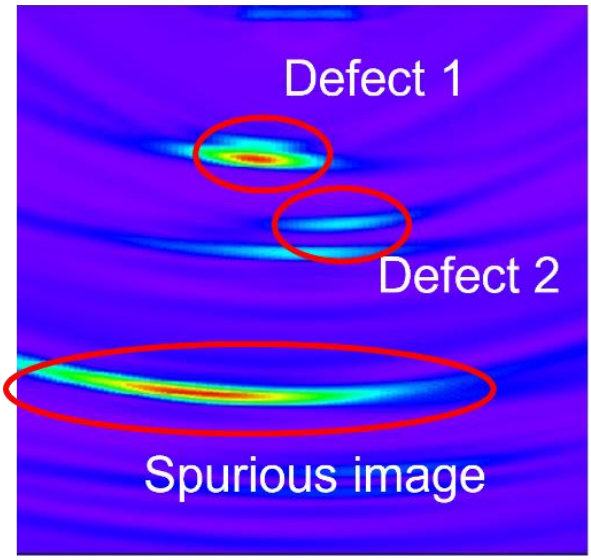

(b) Using a buffer of L = 25 mm

Figure 4.3: Defect imaging without and with a buffer.

4.4 Effective detecting region (EDR)

4.4.1 Theoretical derivation

To avoid image distortion and spurious images, the effective detecting region (EDR) is discussed in this section. For analyzing the EDR, wave distortion by the

dispersion nature of Lamb waves is discussed using the simple expression of the wave velocities of an S0 mode. We now assume that the incident wave from the vibration element is the pulse with the time width of Δt as shown in Fig. 4.4 (a), and that its frequency spectrum has the bandwidth of Δf in the frequency range as in Fig. 4.4 (b). The maximum speed of $c_{\max}$ and minimum speed of $c_{\min}$ are found in the group velocity dispersion curve in Fig. 4.1 in the frequency range. Because the propagating velocities of the S0 mode varies with frequency, the waveform shown in Fig. 4.4 (a) can be distorted and spread as it propagates. After propagating at the distance of l in the plate, the pulse wave in Fig. 4.4 (a) is distorted and the time duration of the wave at the propagation distance of L is ranging from $l/c_{\max}$ to $l/c_{\min} + \Delta t$ as shown in Fig. 4.4 (c).

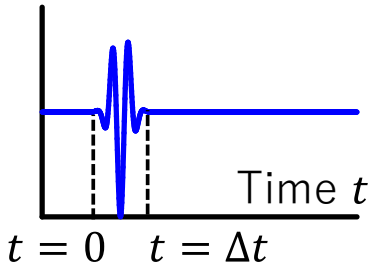

(a) Incident pulse

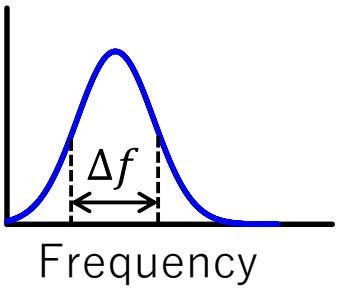

(b) Frequency spectrum of (a)

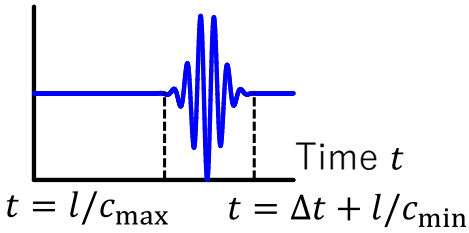

(c) Waveform at the plate end

Figure 4.4: Schematic to show the distortion of incident pulse propagating in a thin plate.

Considering the imaging with PWI with the stacked plate buffer, all the elements emit the signal with no delay and a plane wave is generated in the specimen. The echoes from a defect are individually received by each element. In this condition, it is natural to assume that the incident plane wave can propagate only the region extending straight out from the stack plate buffer. Assume that the distance between the surface of the specimen and the defect (or the position where the intensity value will be acquired in the image) is a, the farthest end of the buffer from the defect is b, the length of the buffer plate is L, as shown in Fig. 4.5, and the sound velocity in the specimen is c. Fig. 4.6 shows the waveforms at the two elements. (a) is at the element which is attached to the buffer plate at the nearest plate from the defect, and (b) is for the farthest plate from the defect. In both cases, the reflected waves from the interface between the stacked plate buffer and the specimen which is one-round-trip echo and two-round-trip echo, respectively, are received at the same time. Between these two reflected waves, the defect echo can be seen at a time different from the time the two reflected waves are received. The beginning and ending time of these echoes are shown in these figures, following the simple representation of wave dispersion as shown in Fig. 4.4. To avoid the overlapping of the echo from defect and the reflected waves from the interface in Fig. 4.6 (a), the following equation should be satisfied:

$$2L/c_{min} + \Delta t < 2L/c_{max} + 2a/c, \tag{4.2}$$

$$2L/c_{min} + 2a/c + \Delta t < 4L/c_{max}. \tag{4.3}$$

Meanwhile, in Fig. 4.6 (b), the following equation should be satisfied:

$$2L/c_{min} + \Delta t < 2L/c_{max} + (a+b)/c, \tag{4.4}$$

$$2L/c_{min} + (a+b)/c + \Delta t < 4L/c_{max}. \tag{4.5}$$

The following set of equations can be found after simplifying the Eqs. (4.2)-(4.5):

$$2L/c_{min} + \Delta t < 2L/c_{max} + 2a/c, \tag{4.6}$$

$$2L/c_{min} + (a+b)/c + \Delta t < 4L/c_{max}. \tag{4.7}$$

Then, a and b can be expressed as:

$$a > c(L/c_{min} - L/c_{max} + \Delta t/2) \equiv a_0, \tag{4.8}$$

$$b < c(4L/c_{min} - 2L/c_{max} - \Delta t) - a. \tag{4.9}$$

In the case of $a < b$, the Eq. (4.5) can be expressed as:

$$b < c(2L/c_{min} - L/c_{max} - \Delta t/2) \equiv b_0. \quad (4.10)$$

Summarizing Eqs. (4.8) and (4.10), the effective detecting region for PWI can be represented as the region surrounded by the red lines in Fig. 4.7.

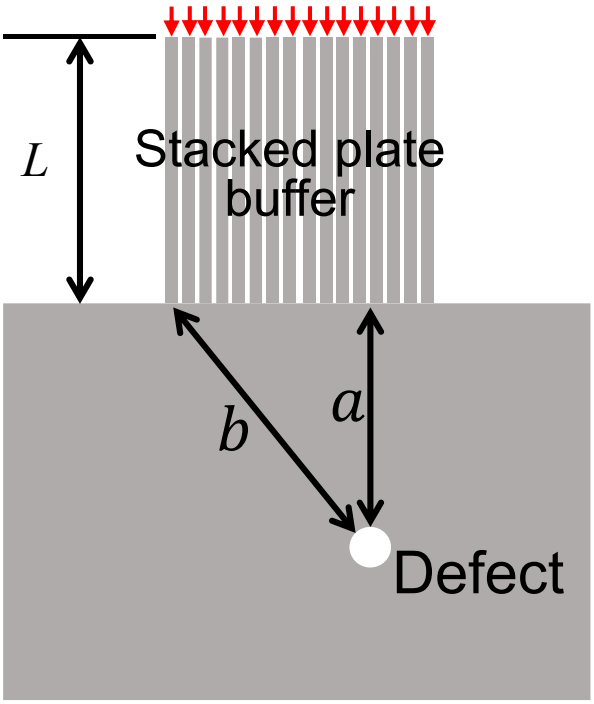

Figure 4.5 Model to show the effective detecting region for PWI.

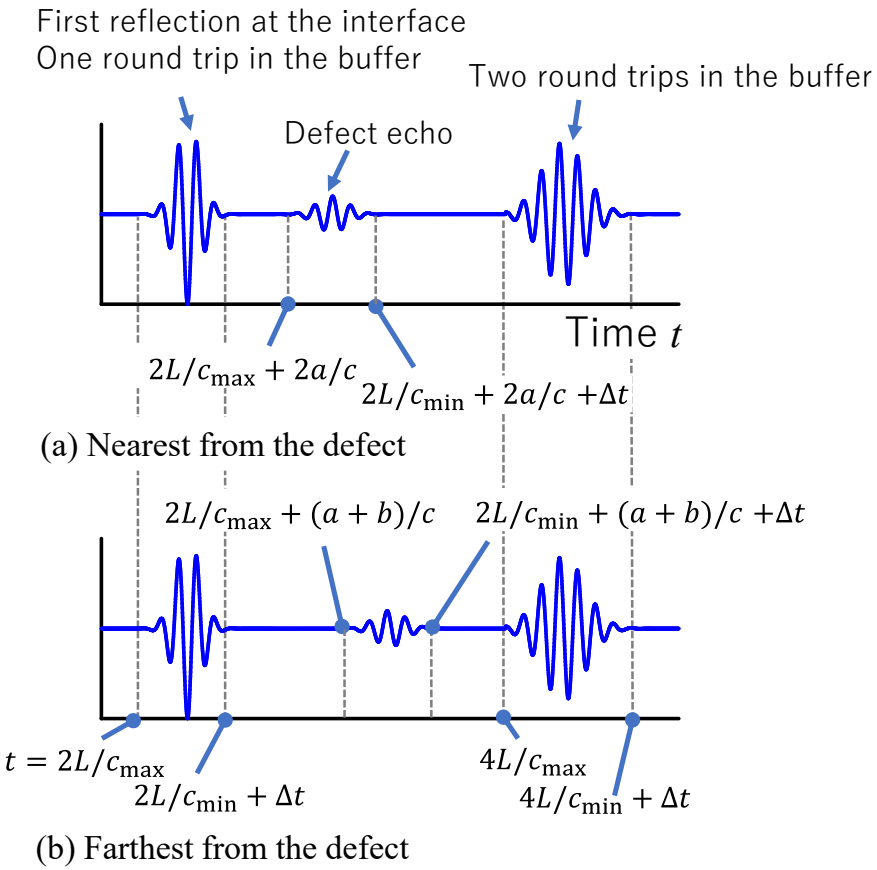

Figure 4.6 Typical waveforms at the two elements, one is the element attached to the plate nearest from the defect, and the other is the element attached to the plate farthest from the defect when PWI is used.

In the case of FMC/TFM, the waveform emitted from a single element is reflected and all elements receive the reflected waves. FMC/TFM can image not only the straight region extending from the buffer width, but also the region outside of it. Assuming that the distance between farthest plate from the defect is b and the closest plate from the defect is a as shown in Fig. 4.8, these are limited by the same equations as Eqs. (4.8) and (4.10). However, the definition of a is different from Eqs. (4.8) and (4.10), and the EDR is represented as in Fig. 4.9. It should be noted that the first reflections from the interface are not exactly the same in Fig. 4.6. If the incident and receiving elements are different, diffracted waves are expected to be measured instead of the first reflected wave in Fig. 4.6. Similarly, the two-round trips will also be slightly different, but we consider their effects to be small, and we have assumed here that it should be the same as in Eqs. (4.8) and (4.10).

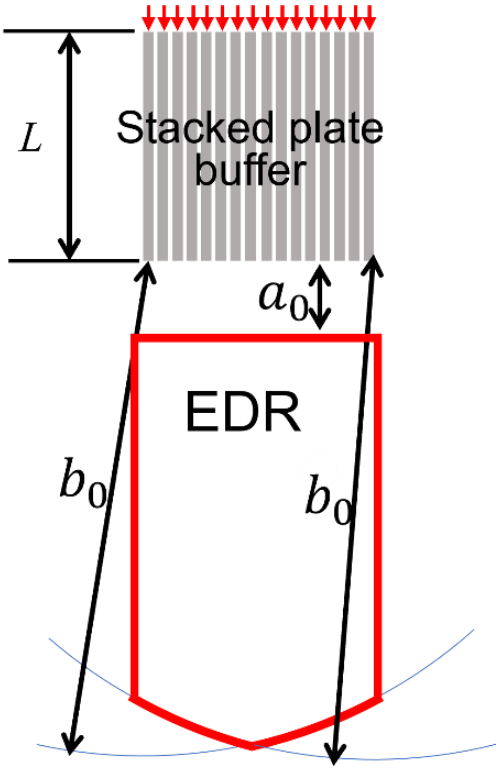

Figure 4.7. The effective detecting region (EDR) for PWI.

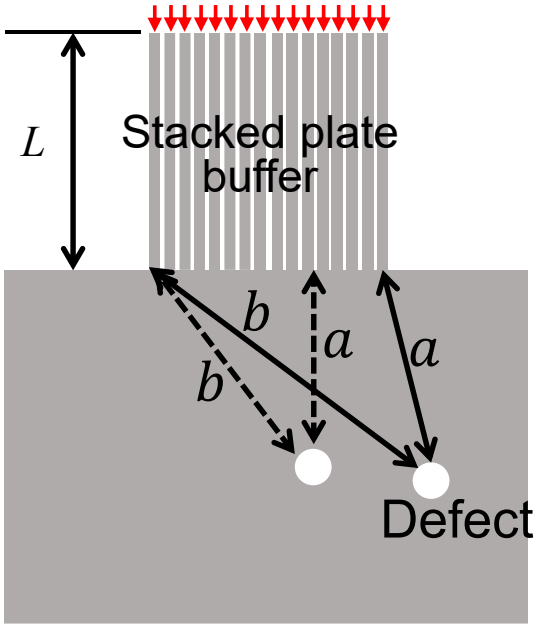

Figure 4.8. Model to show the effective detecting region for FMC/TFM.

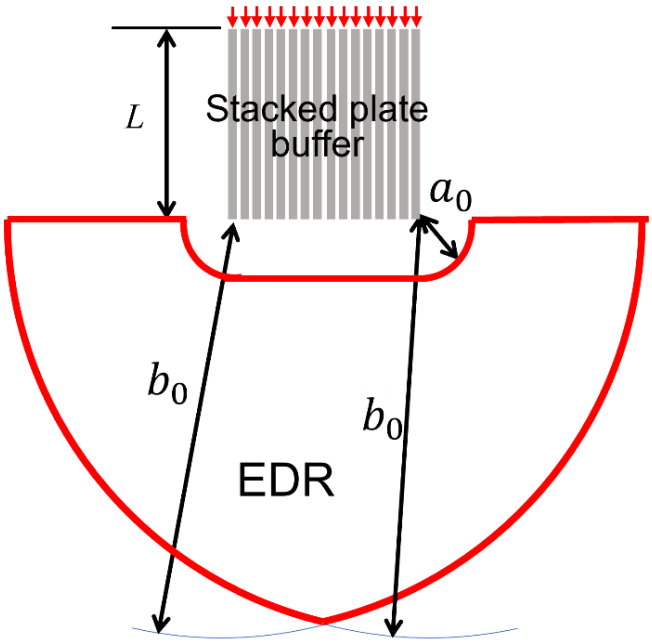

Figure 4.9. The effective detecting region in FMC/TFM.

4.4.2 Numerical investigations of EDR

To prove the simple theory of the EDR as described in the previous section, the calculations of the wave propagations and the imaging are conducted. For PWI, the positions of defects on the model are shown in Fig. 4.10 (a). The defects are set near the boundaries of the EDR drawn in red contour. As shown in Fig. 4.10 (a), Defects 1 and 4 are located outside of the EDR with positions of (-12 mm, 11 mm), (3 mm, 33.5 mm), respectively, and Defects 2 and 3, with the positions of (-7 mm, 15 mm), (5 mm, 24 mm), respectively, are within the EDR. Fig. 4.10 (b) is the imaging result with PWI. In the region between stacked plate buffer and the EDR contour, the high intensity image can be seen due to the large first reflection at the interface between the plate buffer and the specimen, which indicates the defects cannot be found in the PWI image in this region as predicted by the EDR. And also, as expected by EDR, Defects 1 and 4 are not visualized in the image and Defects 2 and 3 can be found the image.

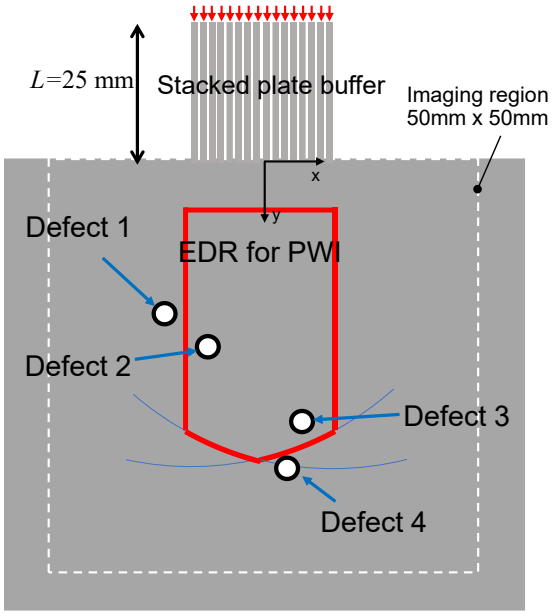

(a) Geometries of the calculation model

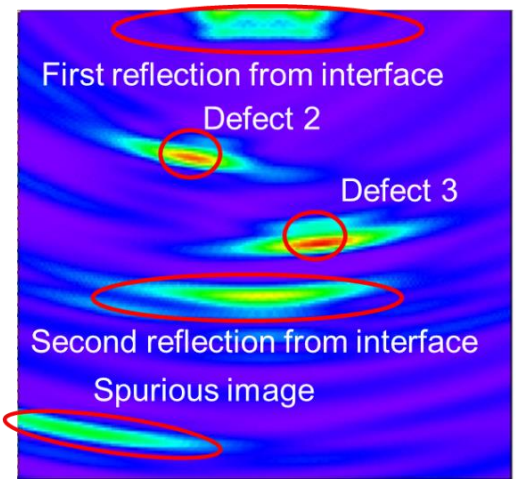

(b) Image with a stacked plate buffer of L= 25 mm

Figure 4.10. Calculation model and result for PWI with a stacked plate buffer.

For FMC/TFM, the defects are set near the boundaries of the EDR drawn in red contour. As shown in Fig. 4.11 (a), Defects 1, 2, 3 and 4 are located outside of the EDR, with the positions of (0 mm, 35 mm), (-12 mm, 28 mm), (-20 mm, 20 mm), (-25 mm, 10 mm), respectively, while other defects, Defect 5, 6, 7 and 8, with the positions of (0 mm, 25 mm), (8 mm, 22 mm), (15 mm, 15 mm), (18 mm, 8 mm) are located within the EDR. The imaging result with FMC/TFM is shown in Fig. 4.11 (b). Different from the result in PWI, in the region between stacked plate buffer and the contour of the EDR, the high intensity image does not appear in this region, which indicates that the first reflected waves do not affect the image so largely as in PWI because incident wave from a single

element reflects back only in the single plate on which the element attached and small refracted waves propagates in the other plates. Defects still can be found in this region using FMC/TFM. And as expected by EDR, Defects 1, 2, 3, and 4 are not visualized in the image, and Defects 5, 6 and 7 can be found in the image. However, Defect 8 cannot be seen in the image even though it is inside the EDR. This is the limitation of beam steering range in phased array transducers due to the directivity property.

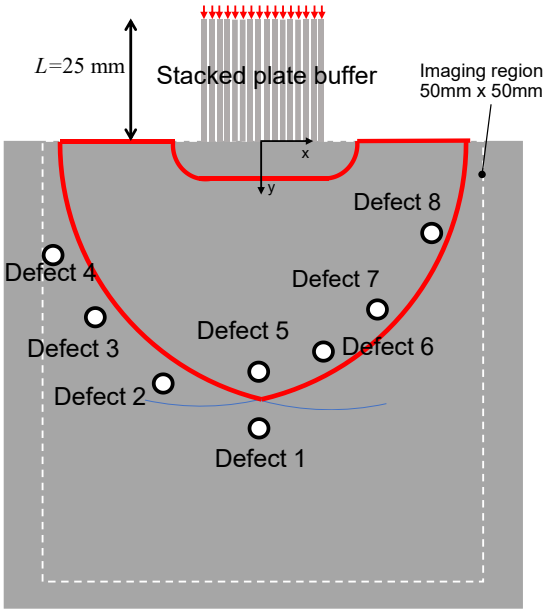

(a) Geometries of the calculation model

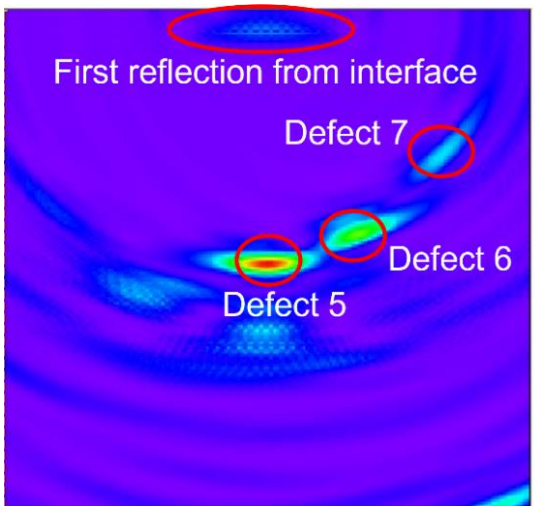

(b) Image with a stacked plate buffer of L= 25 mm

Figure 4.11 Calculation model and result for FMC/TFM with a stacked plate buffer.

4.5 Solution from EDR

According to the theoretical discussions in section 4.4 and the result of the calculations of EDR, the stacked plate buffer is optimized here. From the equations shown in section 4.4, it was derived that the EDR extends in proportion to the buffer length L. To solve the problem mentioned in section 4.2 and in the calculations conducted in section 4.4, imaging simulations with different buffer length L are done in this section for PWI and FMC/TFM. The results for L = 50 mm and 100 mm are shown in Figs. 4.12 and 4.13, respectively, which is double and quadruple of the previous length of buffer in Figs. 4.10 and 4.11. Figs. 4.12 and 4.13 are for PWI and FMC/TFM, respectively. The results of the defect imaging both by PWI and FMC/TFM show that the reflected waves from the interface between the stacked plate buffer and the specimen are removed from the imaging area when using the buffer with length of 100 mm as expected.

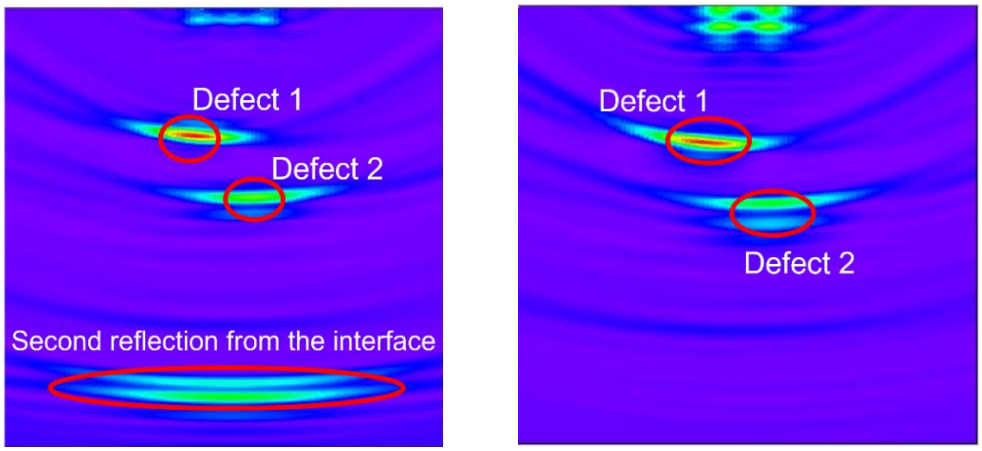

(a) L = 50 mm (b) L = 100 mm

Figure 4.12 PWI images with a stacked plate buffer with different length.

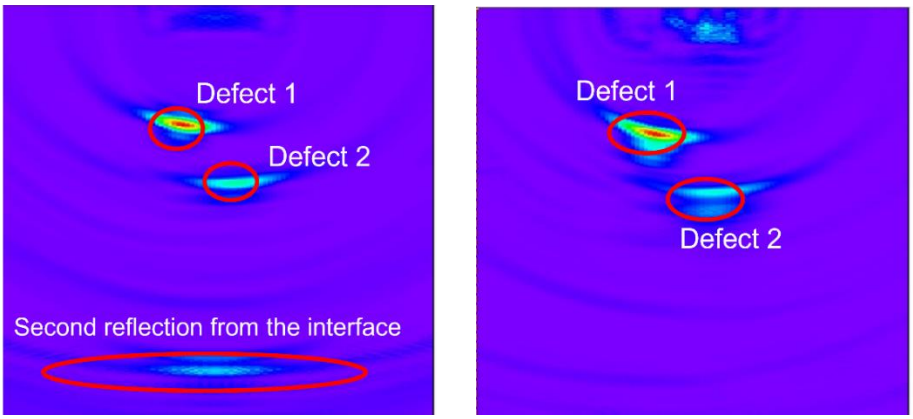

(a) L = 50 mm (b) L = 100 mm

Figure 4.13 FMC/TFM images with a stacked plate buffer with different length.

However, it should be noted that even though the influence from the interface between the stacked plate buffer and the specimen is removed from the imaging area by extending the length of the buffer, the distortion of the waveform of the Lamb wave propagating in the buffer plate due to the dispersion property is not considered. Ultrasonic attenuation due to the damping is not considered in these calculations, either. And there is the limitation of the buffer length due to the Lamb wave dispersion and the ultrasonic attenuation in the practical situation.

4.6 Summary

In this chapter, we proposed a stacked thin plate buffer to solve the problems when using phased array transducer to measure at high temperature. First, we describe the dispersion nature of the A0 and S0 mode Lamb wave at low *fd* range. From the properties of the S0 mode Lamb wave the size of the plates with thickness of 0.9 mm which make up the buffer are decided. Numerical calculations are applied, and the results showed the problem because of the reflection from the interface of the stacked plate buffer and the specimen. Second, the analysis of EDR is illustrated theoretically and show the limitation of the phased array transducer when attached with a stacked plate buffer. Numerical simulations of defect imaging with PWI and TFM agree well with the theoretical illustration. Based on the prediction from EDR, the spurious image of the second reflection from the interface between the buffer and specimen was removed by extending the buffer length.

Chapter 5 Experimental investigation of phased array imaging with stacked plate buffer

5.1 Background

In chapter 4, based on the numerical analyses of the wave propagation in the stacked plate structure, a stacked plate structure was considered instead of a bulk buffer rod as a solution for the PA imaging with a buffer. However, these numerical calculations have some gaps to the validation in real practice.

Firstly, connections of the interfaces between the PA probe and the buffer, buffer and specimen will not be perfect which can be used in numerical calculations. In numerical calculations in chapter 4, the connection between the PA probe and the upper surface of the stacked plate buffer is not considered because the incident signals from the elements of the PA probe are simplified to be a set of longitudinal forces applied on ends of each buffer plate. For the interface between the buffer and the specimen, the buffer plates are perfectly contacted with the surface of the specimen without any gaps, in this condition, the entire structure of buffer and specimen can be regarded as a whole, which is different from this structure used in practice. Thus, for transmitting the signals from each component as much as possible, the method of connection should be considered.

Secondly, for assembling the buffer plates as an entire stacked plate buffer, a type of media should be used between each two plates to attach all plates together and ensure the stability of the structure. However, this media may cause leakage of the wave between different plates and influences results of defect imaging. Thus, the type of the media and the way to attach the plates are very important.

Then the dimension of the numerical calculation is 2D model because the 3D model calculation will be very time and memory consuming. The width of plates of the buffer is not considered. Thus, the purpose of this chapter is to confirm the feasibility of the PA imaging with a stacked plate buffer experimentally.

5.2 Overview of phased array imaging with a stacked plate buffer

Our previous work proved by numerical simulations that PA technology such as beam focusing and defect imaging can be used within the solid material when a stacked

plate buffer is attached to a PA probe, as shown in Fig. 5.1. In this section, the principle of the PA imaging with a stacked plate buffer is briefly explained using Lamb wave dispersion curves.

A stacked plate buffer consists of a series of thin flat plates, the pitch and thickness of which are adjusted so that each piezoelectric element of the PA probe corresponds to an end of single thin plate. When the PA probe is brought into contact with the end of the stacked plate buffer, the vibrations of the individual piezo elements propagate directly through the plate to the opposite end. In other words, even in the presence of a buffer, the object in contact with the buffer can be vibrated, just as if the PA probe were in direct contact with the object. This makes use of the nature of the S0 mode of Lamb wave propagating through the thin plate.

The individual vibrating elements of the PA probe emit longitudinal waves with displacements perpendicular to the vibrating surface, so that vibrations in the longitudinal direction of the thin plate are incident on the edge surface of the thin plate. Because this vibration resembles the vibration distribution of the S0 mode in the cross-section of the thin plate, most of the Lamb modes propagating in the thin plate are the S0 mode. Fig. 5.2 shows the group velocity dispersion curve of Lamb waves for a stainless-steel plate of thickness d with longitudinal and transverse wave velocities of c_L =5790 m/s and c_T =3100 m/s, respectively, where the horizontal axis is represented by the product of frequency f and plate thickness d and the vertical axis by the group velocity. The S0 mode is less dispersive in the low fd region and approaches plate velocity ($c_{plate} = 2c_T\sqrt{1-(c_T/c_L)^2}$ =5236 m/s) at $fd \rightarrow 0$. Considering the S0 mode in the low fd range, the propagating pulse wave reaches the opposite end of the plate with a small change in shape. When these ends are in contact with the object and delays are given to the elements in the PA probe as shown in Fig. 5.1, for example, the delays given are maintained and the ultrasonic pulses propagate almost unchanged. Resultingly ultrasonic focusing can be achieved in the object as shown in Fig. 5.1. Other than the focusing, numerical calculations have shown that PWI and FMC/TFM can also be used to image defects even with a stacked plate buffer, which is shown in chapter 4. In other words, it is expected that ultrasonic PA technology can be used almost without modification by using a thin plate buffer.

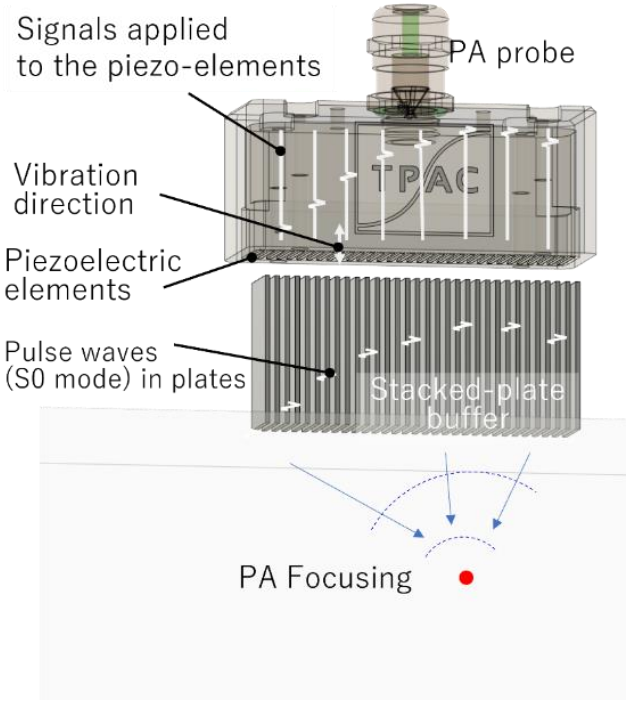

Figure 5.1 Schematic diagram of PA focusing with a stacked plate buffer.

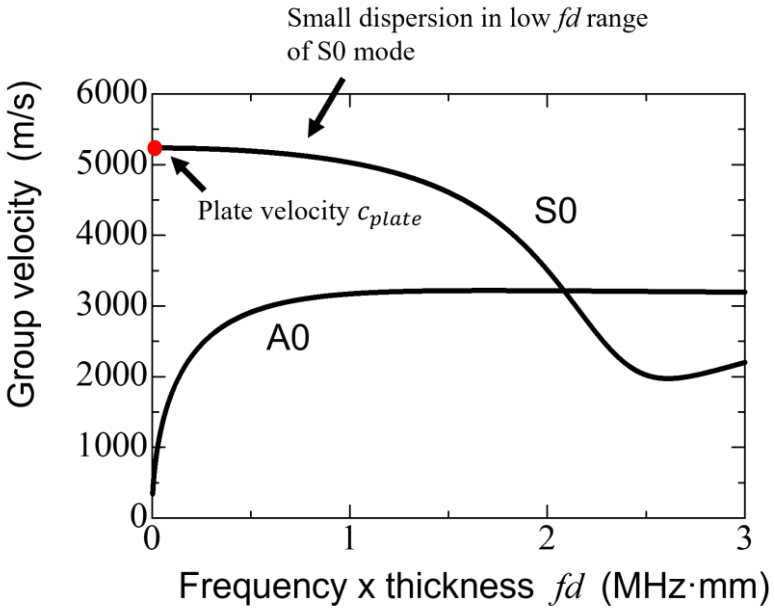

Figure 5.2 Group velocity dispersion curves of Lamb waves in the low *fd* range for the plate with longitudinal and transverse wave velocities of 5790 m/s and 3100 m/s, respectively, and the velocity of S0 mode at *fd*=0, called plate velocity, is 5236 m/s.

5.3 Settings of experiment

The experimental set-up and test specimen for the imaging experiment using a PA probe with the proposed stacked plate buffer are described in this section. In this experimental investigation, a linear array PA probe consisting of 64 elements with an element size of 15 mm × 0.9 mm, a pitch of 1 mm, an element gap of 0.1 mm, and a total aperture of 15 mm × 63.9 mm, is used to collect the experimental data by PWI and FMC. All elements exhibit nearly identical bandwidths with a center frequency of 1.0 MHz and a full width at half maximum of about 1.0 MHz. The array was driven by PA equipment (The Phased Array Company, Explorer). The system uses a 14 bit and 64-channel architecture and can perform the acquisition of all the 64 channels in parallel at a sampling frequency of 50 MHz. In these experiments, the controller was driven from a PC using the LabVIEW interface. Each element of the PA probe can apply longitudinal force on the edge of each buffer plate and incident an ultrasonic pulse wave with the center frequency of 1 MHz into each buffer plate which each piezoelectric element paired with.

Fig. 5.3 shows a picture of the stacked plate buffer and a single stainless-steel (SUS304) plate used in the experiments in this section. The SUS304 plate is 0.9 mm thick, the same thickness as the piezo element of the PA probe, and 100 mm long, the same length of the buffer used in the previous numerical verification shown in chapter 4. The width of the buffer was 50 mm. 64 plates were assembled using a double-sided tape with a nominal thickness of 0.09 mm, which is the closest to 0.1 mm, the gap between the piezoelectric elements of the PA probe, among commercially available double-sided tapes. The gap between the elements of the PA probe and the thickness of the tape was slightly different, but the aperture did not have a large error after assembly. The double-sided tape was 5 mm wide and was applied to the upper side where the PA probe contacts and the bottom side where the object to be inspected contacts, as shown in Fig. 5.3. In addition to the purpose of attaching the plates, the tape was also used to prevent the couplant applied to the upper and lower edges from penetrating between the thin plates. The area where the double-sided tape is attached to the plate was small to minimize crosstalk, which is the propagation of waves through the double-sided tape to the plate next to it. Since a longitudinal wave with a center frequency of 1 MHz was incident on the upper surface of the plate, S0 mode of Lamb waves, which has a similar vibration form to the longitudinal wave, propagates significantly in the thin plate. Considering that the plate thickness is 0.9 mm, and fd = 0.9 MHz-mm, the S0 mode propagates in the small dispersion range as shown in Fig. 5.2.

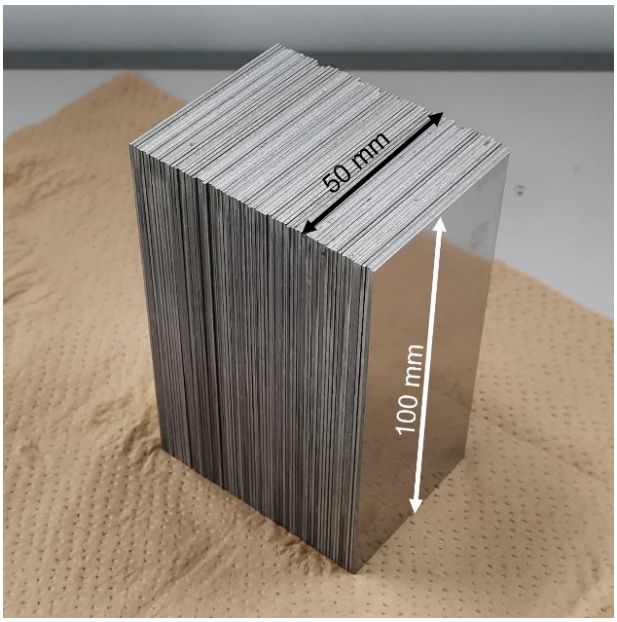

(a)

(b)

Figure 5.3 Pictures of (a) a stacked plate buffer has been formed by buffer plates, and (b) a single buffer plate attached by tapes before attached with other buffer plate.

As shown in Fig. 5.4, the aluminum alloy (A5052) specimen is a 100 mm × 100 mm × 50 mm rectangular solid having three side drilled holes (SDH). The SDHs #1, #2, and #3 located 20 mm, 25 mm, and 30 mm from the upper surface, and 20 mm, 40 mm, and 60 mm from the left surface, respectively. The diameter of # 1 and #3 are 3.0 mm, while the diameter of #2 is 3.5 mm. Waveforms were collected and processed in two-different ways, PWI and FMC/TFM, for defect imaging.

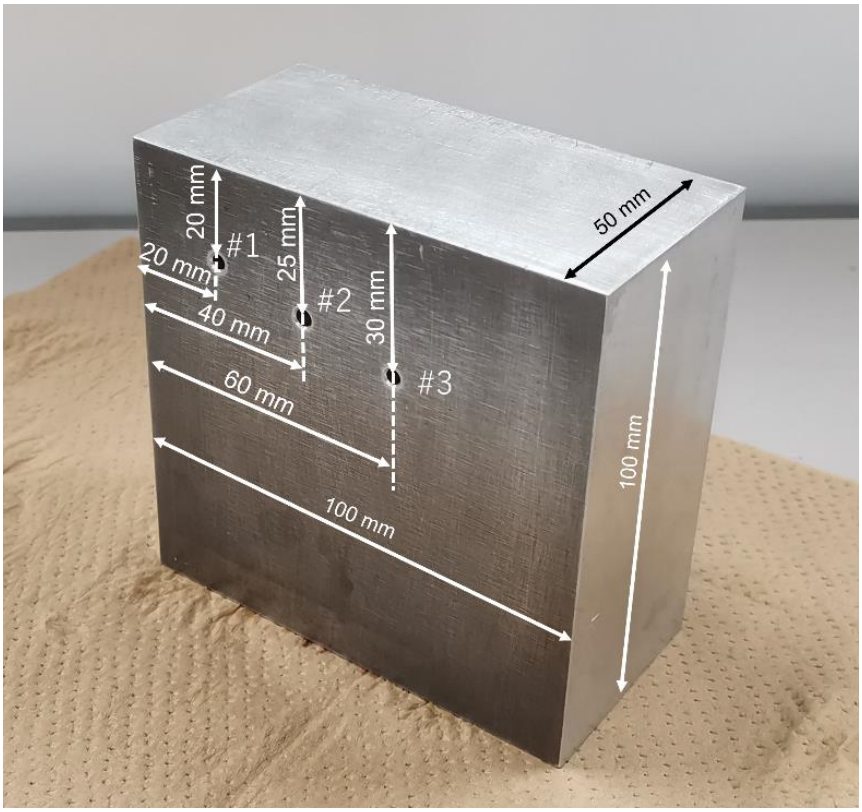

Figure 5.4 A picture of the specimen with three SDHs as internal reflectors to test the effectiveness of the stacked plate buffer.

Before imaging experiments with a stacked plate buffer, imaging experiments were done by the PA probe without the buffer as shown in Fig. 5.5 (a). After confirming defect images can be obtained with the PA probe, imaging experiments with a stacked plate buffer were done as shown in Fig. 5.5 (b). In all experiments, a regular couplant for longitudinal waves was applied between the PA probe and specimen, PA probe and buffer, and buffer and specimen. In actual inspections at high temperatures, it is necessary to use adhesives or couplant that can be used at the high temperatures expected. The imaging areas, regions of interest (ROI), were the squares of 60 mm × 60 mm shown in the Fig. 5.5. The upper and lower edges of the stacked plate buffer were attached to the PA probe

and the upper surface of the specimen, respectively. A coupling medium for longitudinal wave probes was applied to these contact surfaces.

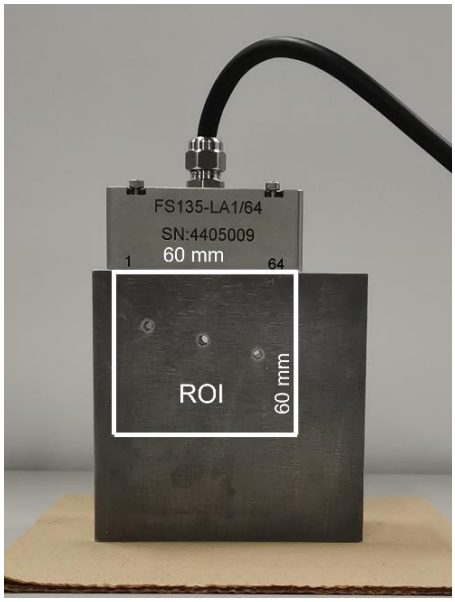

(a)

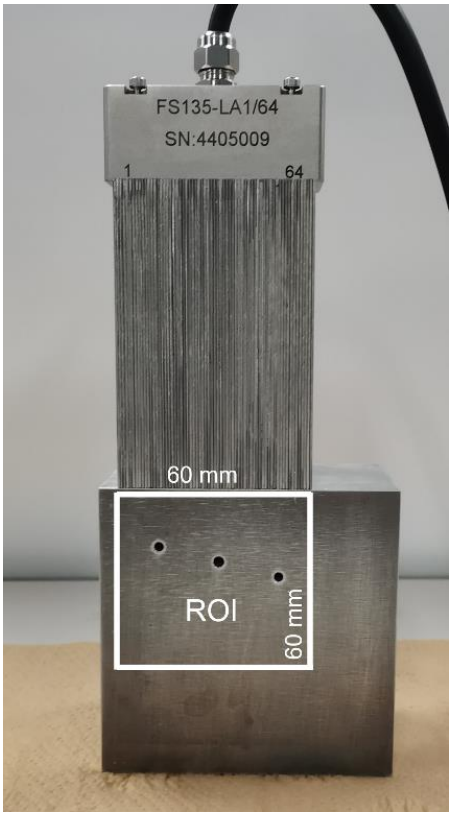

(b)

Figure 5.5 Pictures of the experimental devices and specimen when (a) phased array probe without a stacked plate buffer, and (b) with the stacked plate buffer.

5.4 First experiment and trailing wave

5.4.1 Result of experiment

Fig. 5.6 shows the defect images in the first experiments using the PA probe with and without the buffer shown in Fig. 5.3. Defect images were obtained using the PWI and FMC/TFM without buffer as shown in Fig. 5.6 (a) and (b), respectively. Then, the defect images were obtained using the PA probe with the buffer as shown in Fig. 5.6 (c) and (d). These imaging processes were performed assuming that the S0 mode with a phase velocity of 5100 m/s propagate in the buffer and longitudinal waves with a velocity of 6400 m/s propagate in the aluminum specimen. The colors of the images represent intensities calculated by the PWI or TFM, normalized by the maximum intensity of each figure. In Fig. 5.6 (a) and (b) without a buffer, clear SDH images were obtained at the appropriate positions. However, in Fig. 5.6 (c) and (d) using the buffer, the SDH images were blurred because high intensity areas appear around 40 mm from the top. The reason for this high intensity area is discussed in the next section using numerical calculations.

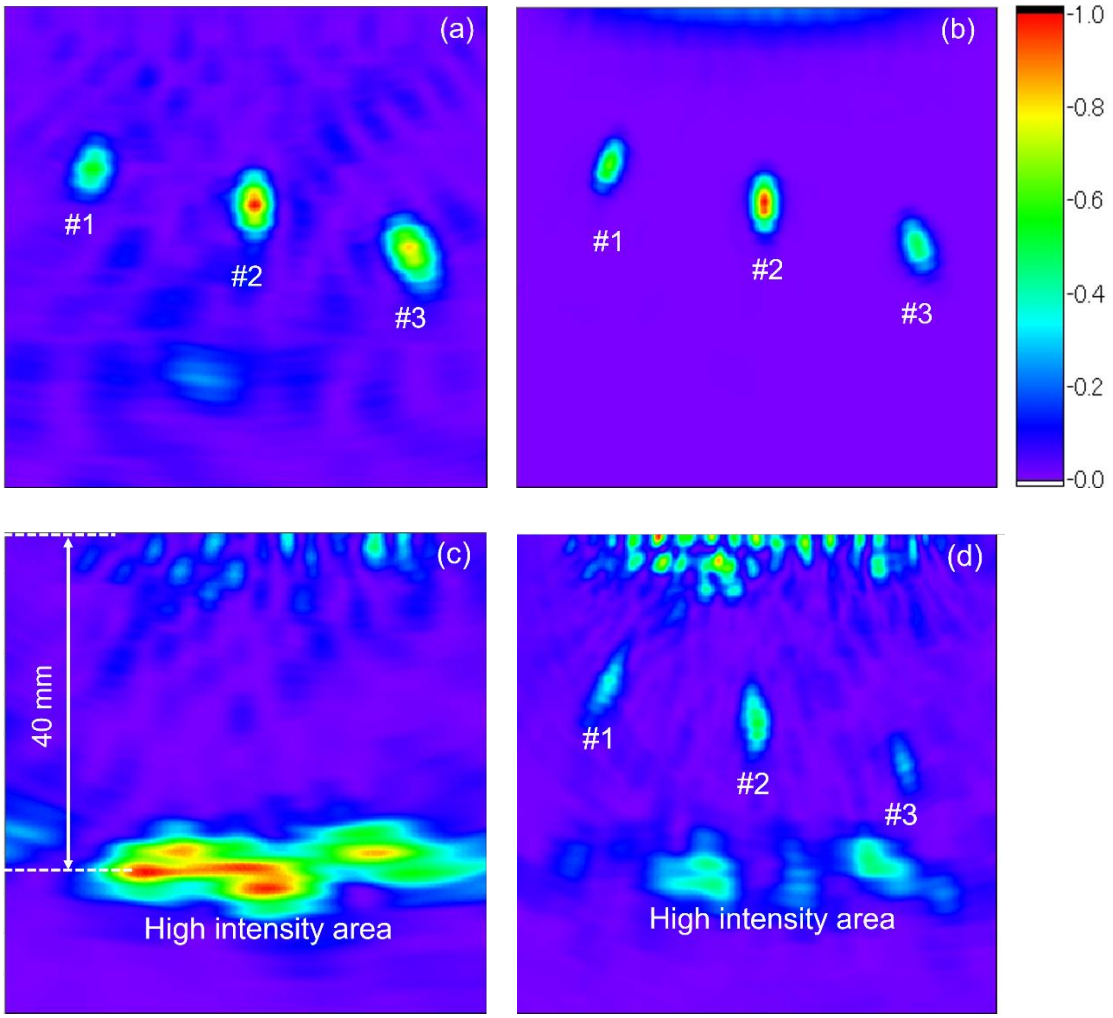

Figure 5.6 Defect images when using the PA probe with and without the stacked plate buffer. (a) PWI and without buffer. (b) FMC/TFM without buffer. (c) PWI with buffer. (d) FMC/TFM with buffer.

5.4.2 Numerical analysis to investigate the cause of spurious images

To investigate the cause of the high intensity areas, numerical calculations of wave propagation in a thin plate were carried out in this section. Considering the plate is thin, two-dimensional calculations were done under the plane stress condition by COMSOL Multiphysics®. Although this assumption may not adequately represent the

dispersion of Lamb waves, it was sufficient to identify the cause of the problem here, saving significant computation time and memory. Firstly, the wave propagation in a 100 mm × 50 mm plate was investigated. Two-dimensional plane stress calculation was performed by applying the vertical dynamic normal force to the width of 15 mm at the upper end of the plate with a center frequency of 1 MHz to simulate the dynamic force from the PA probe used in the experiments. All boundaries around the rectangular thin plate were assumed to be traction free boundaries. Fig. 5.7 shows the snapshots of the propagating waves at four different time steps: (a) 9 μs just after the dynamic normal force is applied at the upper end, (b) 19 μs when the incident wave arrives at the lower end of the plate, (c) 39 μs when the main straight wave packet reaches the upper end of the plate, (d) 52 μs when a trailing wave reaches the upper end of the plate. As shown in Fig. 5.7 (a), the incident wave from the top of the plate spreads as it propagates. Then the spreading incident wave reflects and generates mode converted shear horizontal (SH) waves at both side edges, and the mode converted SH waves appear as oblique lines from both side edges behind the main straight propagating wave packet, as shown in Fig. 5.7 (b). At the end of the oblique lines, the horizontally straight wave can be seen, as shown in 5.7 (c). This is known as trailing waves [77], which appears with the interval from the main straight wave described as the following equation:

$$\Delta t_{plate} = \frac{w}{c_T \cos \alpha} - \frac{w}{c_{plate}} \tan \alpha \,, \tag{5.1}$$

where w, c_T, c_{plate} are the width of the plate, transverse wave velocity, a plate wave velocity, respectively, and α is $\sin^{-1}(c_T/c_{plate})$. In the case of the bulk wave propagation in a plate with the thickness of w and the infinite width, longitudinal wave velocity c_L should be used instead of c_{plate}. In Fig. 5.7 (c), this trailing wave arrives at the upper end approximately 13 ms after the first main straight wave packet, which agrees well with Eq. (5.1). This travelling time corresponds to a propagation distance of about 80 mm inside the test specimen, which indicates the cause of the high intensity areas in Fig. 5.6 (c) and (d) is the trailing wave that behaved as if the reflectors were located 40 mm from the upper surface of the test specimen.

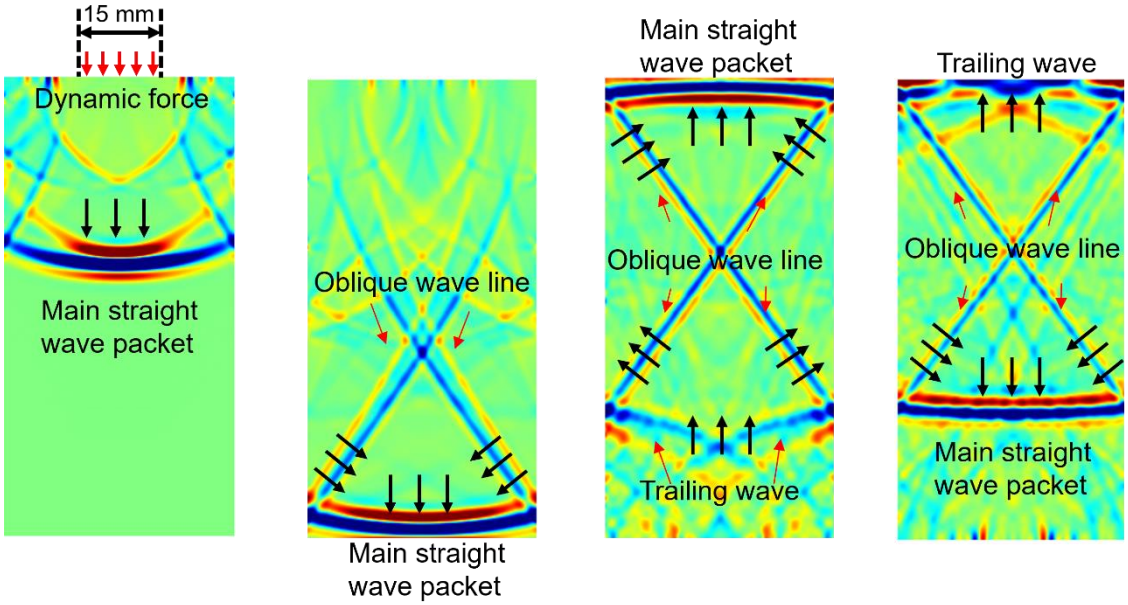

(a) (b) (c) (d)

Figure 5.7 Snapshots of wave propagation in a plate with 100 mm×50 mm plate at (a) 9 μs after the dynamic normal force is applied at the upper end, (b) 19 μs when the incident wave arrives at the lower end of the plate, (c) 39 μs when the main straight wave packet reaches the upper end of the plate, (d) 52 μs when a trailing wave reaches the upper end of the plate. The color represents the displacement in the vertical direction. The black arrow represents the direction of the wave propagation.

To solve the problem of high intensity areas caused by the trailing wave shown in Fig. 5.7, buffer plates with different widths were used to investigate the relation between the width of the buffer plate and the travelling time of the trailing wave. Two-dimensional plane stress calculations were performed under the same conditions as in Fig. 5.7, except the width of the plates. Calculations were carried out for 30 mm, 70 mm, and 100 mm wide plates. Fig. 5.8 shows the snapshots of the wave propagation in three buffer plates with different widths at the time step when the main straight wave packet reaches the upper end of the plate. As shown in Fig. 5.8 (a) for a 30 mm wide plate, the trailing wave arrives at the upper end about 8 ms after the first main straight wave, which corresponds to a propagation distance of about 50 mm inside the test specimen and can produce a high intensity area located about at 25 mm from the upper surface of the test specimen. As shown in Fig. 5.8 (b) and (c), for 70 mm and 100 mm wide plates, respectively, the trailing waves were not observed in the snapshots when the main straight wave packet reaches the upper end of the plate. In this condition, the time of the trailing wave arrives at the upper end of the buffer plate will be more than 18 ms after the main

straight wave packet. Comparing the snapshots shown in Fig. 5.7 (c) and Fig. 5.8, we can draw the conclusion that the time gap between the main wave packet of the reflected wave and the trailing wave becomes larger by expanding the width of the buffer plate, where the high intensity area shown in Fig. 5.6 (c) and (d) can be farther away from the ROIs.

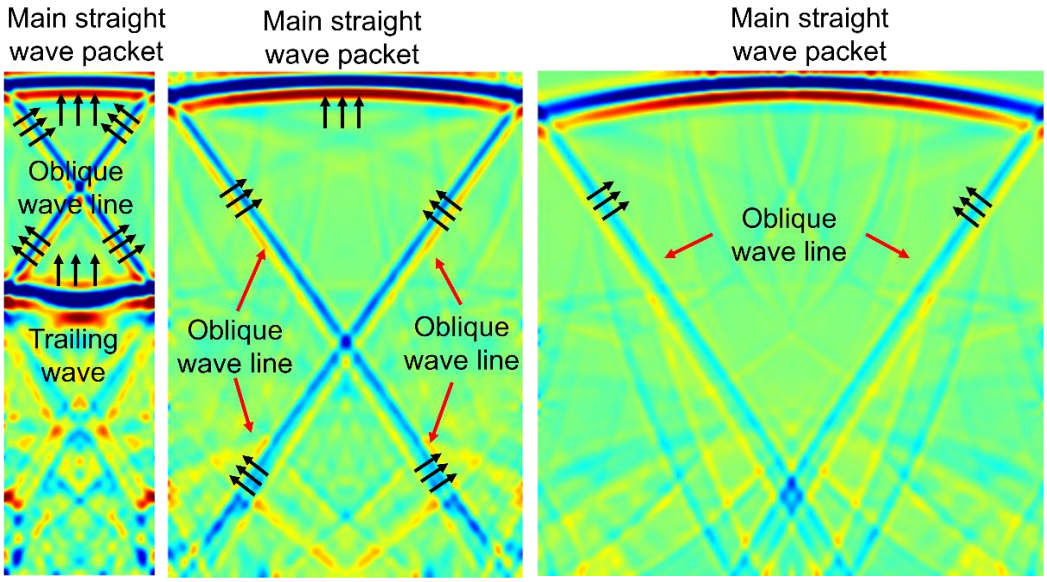

(a) (b) (c)

Figure 5.8. Snapshots of the wave propagation for (a) 30 mm, (b) 70 mm and (c) 100 mm wide plates. All the snapshots show the waveforms at 39 μs when the main straight wave packet reaches the upper end of the plate.

5.5 Experiments using stacked plate buffers with different widths

To test the performances of the stacked plate buffers consisting of 30 mm, 70 mm, and 100 mm wide plates, imaging experiments were conducted. All the buffer plates are 100 mm long and 0.9 mm thick. The preparation of the stacked plate buffers and the experimental process are the same as done in 50 mm width buffer, described in Section 2. The same specimen was used in the experiments. Fig. 5.9 shows the imaging results: (a) and (b) for 30 mm wide plate, (c) and (d) for 70 mm wide plate, and (e) and (f) for 100 mm wide plate, respectively, and (a), (c), (e) were created by PWI, and (b), (d), (f) were created by FMC/TFM, respectively. For 30 mm wide plate in Fig. 5.9 (a) and (b), high intensity areas are shown in the ROIs around 25 mm and 50 mm from the top. Defect images cannot be observed due to the high intensity areas. The high intensity areas around

25 mm from the top were created by the trailing wave as described in the previous section, that is, Δt = 8 μs for a 30 mm wide plate and this corresponds to the roundtrip distance of 25 mm in the test specimen. Because the trailing waves appears repeatedly at intervals of Δt, the high intensity areas around 50 mm from the top were created by the second trailing wave. Comparing Fig. 5.9 (a) and (b), it can be seen that the high intensity area in (a) of PWI is wider and greater than that in (b) of FMC/TFM. This is due to the difference in signal processing between PWI and FMC/TFM. In PWI, pulse waves are incident simultaneously from all piezoelectric elements and received by all of them, where all of the received signals include the trailing waves reflected from the buffer plate end, and the signals including these trailing waves are processed to obtain an image of the inside of the test specimen. On the other hand, FMC/TFM repeats the measurements in which the incident wave outputs from one piezoelectric element and all piezoelectric elements receive the reflected waves. When the incident element and the receiving element are the same, the received signal contains trailing waves in the buffer plate, but the other received signals, in which the incident and receiving elements are different, contain very small trailing waves that have come around through the test specimen. The influence of trailing waves is reduced in FMC/TFM because these received waveforms are processed and imaged. When the width of the buffer plates expanded to be 70 mm, shown in Fig. 5.9 (c) and (d), the images of the SDHs are clearer compared with the imaging results for 50 mm wide plate shown in Fig. 5.6 (c) and (d). Only small horizontal area can be seen at the bottom of the ROIs, due to the trailing wave. In this condition, the influence from the trailing wave to the imaging result decreases compared with results for narrower plates. For 100 mm wide plate, as shown in Fig. 5.9 (e) and (f), the high intensity areas caused by the trailing wave are totally removed from the ROIs. And therefore, images of the SDHs are clearer than those using narrower plates. Summarizing the experimental results in Fig. 5.9, the high intensity spurious areas caused by the trailing waves in the stacked plate buffer can be removed using wider buffer plates.

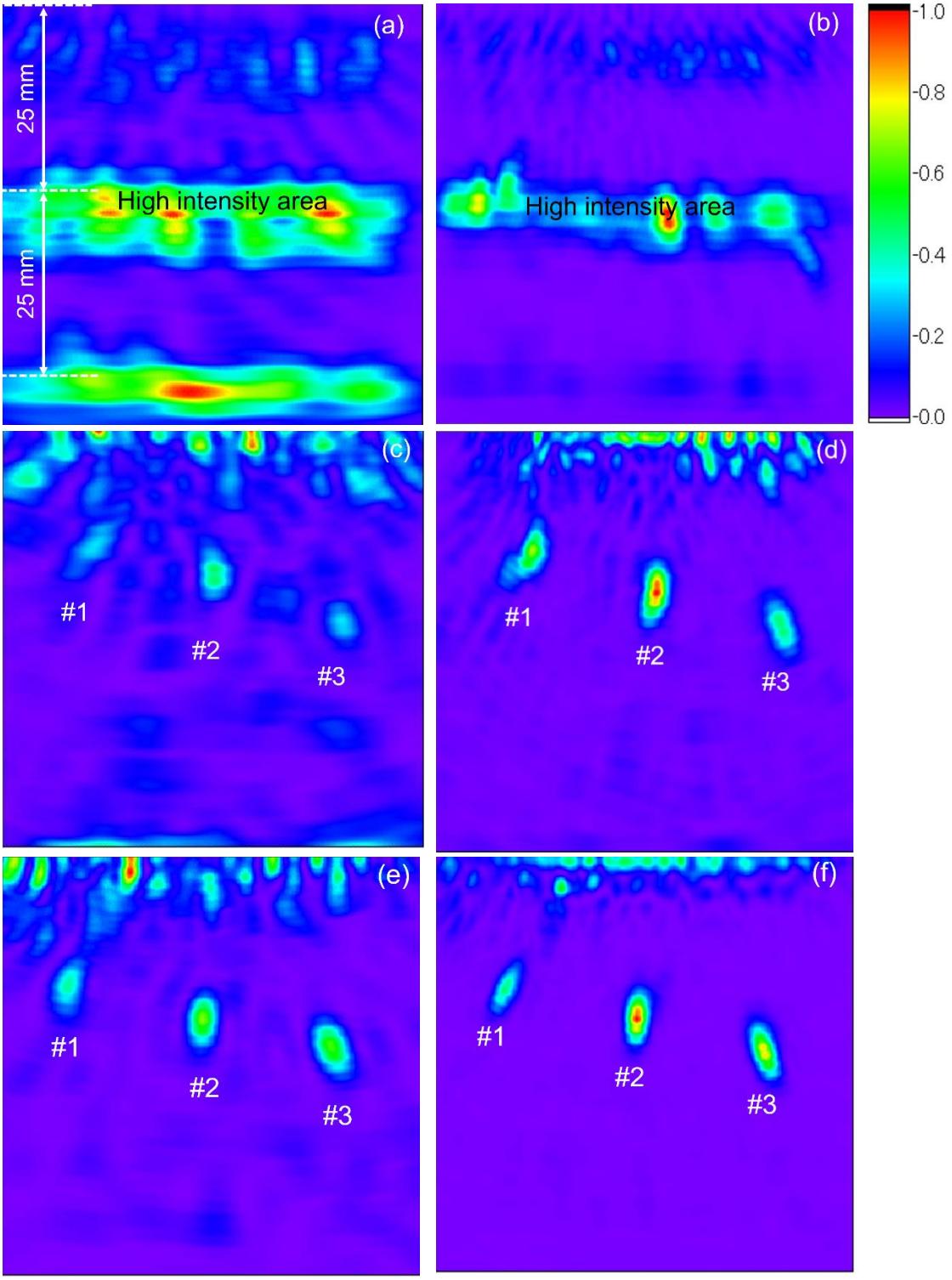

Figure 5.9 Defect images using the PA probe with the stacked plate buffer with different widths and different imaging processes. (a) 30 mm wide buffer and PWI. (b) 30 mm wide buffer and FMC/TFM. (c) 70 mm wide buffer and PWI. (d) 70 mm wide buffer and FMC/TFM. (e) 100 mm wide buffer and PWI. (f) 100 mm wide buffer and FMC/TFM.

5.6 Summary

The feasibility of defect imaging using a PA probe attached with a stacked plate buffer was experimentally investigated. SDHs in an aluminum specimen were imaged using a linear array probe with 64 elements at a center frequency of 1 MHz and a stacked plate buffer consisting of a 0.9 mm thick, 100 mm long SUS plate. In the case of the buffer with a 50 mm wide plate, large spurious images appeared in the defect image. Numerical simulations proved that this was caused by trailing waves originating from SH waves due to mode conversion at the both sides of the plate, and the results agreed well with previous theoretical studies. In order to reduce the influence of the trailing waves on defect images, a wider plate was used, and a very clear defect image was obtained.

Chapter 6 Buffer consisting of a bundle of circular cylinders

6.1 Use of circular cylinder bundles for phased array buffers

The previous chapters proved using numerical simulations and experiments that PA defect imaging is feasible when a buffer consisting of a bundle of thin flat plates is attached to a PA probe. All waves propagating in plates maintain their waveforms and time delays due to small dispersion characteristic of S0 mode of Lamb waves in low frequency-thickness (*fd*) product range, and therefore the stacked plate buffer can extend the imaging range compared to the bulk buffer rod. However, these studies showed that there are two limitations to the use of the stacked plate buffer. One is the limitation of imaging area due to multiple reflections at both ends of the buffer, and the other is generation of spurious images due to trailing waves caused by mode converted waves at both side walls of the plates. Although the first limitation is inevitable as long as buffers are used for phased array imaging, the second one about trailing wave was solved in chapter 5 by expanding the width of the buffer plate.

In this chapter, an alternative way to solve the issue of trailing waves is proposed by using circular cylinders. The method of eliminating trailing waves from the waveguide can be explained qualitatively from the theory of generation of trailing waves and more precisely from the theory of propagation of guided waves in a circular cylinder, as follows.

Trailing waves in a flat plate with finite width are generated by mode conversion that occurred at the sides. An S0 mode of Lamb wave propagates in a plate and the spread wave reflects at the side walls, causing some mode conversion, resulting in shear horizontal waves. In such case, due to differences in the propagation distance and propagation speed, it is known that even if a single longitudinal pulse wave is incident on the end of the buffer material, multiple trailing waves are observed on the opposite side of the buffer material with a certain time interval following the incident main straight wave pocket.

In the previous chapters of stacked plate buffer, we analyzed the trailing wave in the case of a thin plate of finite width in a thin plate in plane stress condition. If the width of the thin plate used as the buffer material is w, the sound velocity of the S0 mode and the transverse wave velocity in the thin plate are c_{plate} and c_T, respectively, and the reflection angle when the mode conversion from the S0 mode to the SH wave occurs is α, then the interval at which the trailing wave appears, Δt_{plate}, can be expressed as [77]:

$$\Delta t_{plate} = \frac{w}{c_T \cos \alpha} - \frac{w}{c_{plate}} \tan \alpha \,. \tag{6.1}$$

Based on Eq. (6.1), increasing the width of the thin plate w leads to longer time interval Δt_{plate}, and resulting elimination of the influence of the trailing wave from the imaging area.

The interval of the trailing waves for a circular cylinder can be calculated in the same way. The interval after which the trailing waves appear, $\Delta t_{cylinder}$, can be expressed as:

$$\Delta t_{cylinder} = \frac{D}{c_T \cos \beta} - \frac{D}{c_L} \tan \beta \,, \tag{6.2}$$

where D is the diameter of the circular cylinder, c_L and c_T, are the longitudinal wave velocity and the transverse wave velocity in the circular cylinder, respectively, and β is the reflection angle when the mode conversion from longitudinal wave to transverse wave occurs at the cylinder side wall.

Therefore, as with the thin plate, by increasing the diameter of the circular cylinder and delaying the arrival time of the trailing wave, it is possible to eliminate its influence outside the imaging area, or conversely, by reducing the diameter of the circular cylinder and shortening the interval of the trailing wave, it is possible to concentrate the trailing wave closed to the main straight wave pocket, which will be used in this study.

To accurately analyze wave propagation in a circular cylinder, the wave field must be considered as guided waves. Fig. 6.1 shows the group velocity dispersion curves for a stainless-steel circular cylinder with longitudinal sound velocity 5790 m/s, transverse sound velocity 3100 m/s, used in later experiments. The dispersion curves were obtained by the semi-analytical finite element method. The horizontal axis is the frequency (f)×circular cylinder diameter (D), and the vertical axis is the group velocity (c_g). The mode with the largest group velocity represents the mode of longitudinal vibration, which can be generated by excitation in the vertical direction from the cross-section of the circular cylinder. The longitudinal vibration mode has low dispersion in the low fD range and can be used as buffers in the same way as thin plates. Namely, pulse wave generated at the one end of a circular cylinder can reach the opposite end with nearly the same waveform.

Considering the use of circular cylinders as a PA buffer, the configuration is as shown in Fig. 6.2. The pitch and diameter of a buffer consisting of a bundle of circular cylinders are adjusted so that each piezoelectric element of the PA probe corresponds to the end of a bundle of circular cylinders. Vibrations of the individual piezoelectric elements can propagate through each circular cylinder to the other end when the PA probe

contacts with the end of the buffer consisting of a bundle of circular cylinders. In other words, the presence of the buffer can still transmit the vibrations from the PA probe and the object contact with the end of the buffer can be vibrated, as if the PA probe directly contact with the object. The nature of guided wave propagating through the circular cylinder is used.

Each vibrating element of the PA probe generates longitudinal waves with displacements normal to its surface, causing vibrations along the axial direction of the circular cylinders to incident on their edge surfaces. Since this vibration pattern resembles that of the first longitudinal mode in the cross-section of the cylinder, the dominant propagating wave mode within the circular cylinder is the first longitudinal mode.

When the ends of the circular cylinders are in contact with the object and delay laws are applied to the PA probe elements as illustrated in Fig. 6.2, the delays and ultrasonic pulses remain nearly unchanged at the opposite ends. Therefore, a buffer composed of bundle of circular cylinders allows the ultrasonic phased array technique to be used with minimal modification.

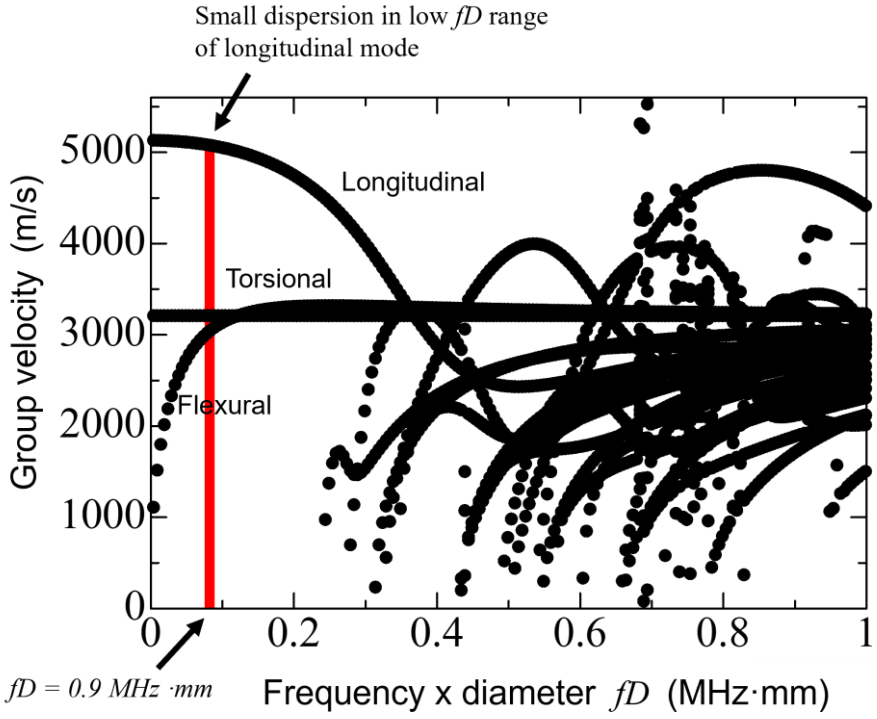

Figure 6.1 Group velocity dispersion curves of guided waves for a circular cylinder with longitudinal and transverse wave velocities of 5790 m/s and 3100 m/s, respectively.

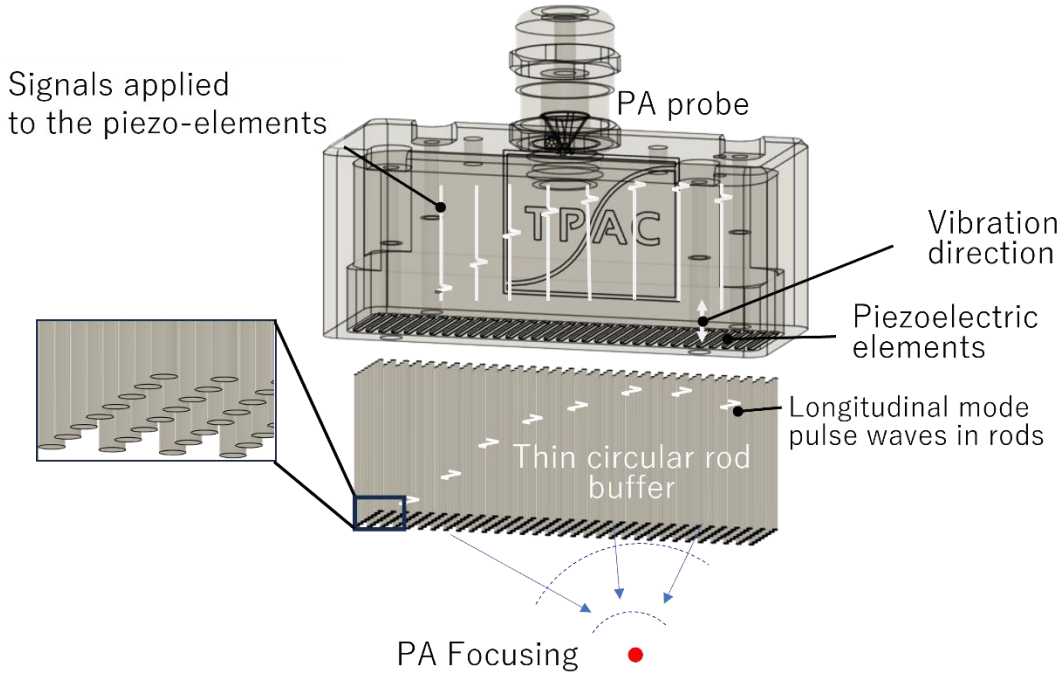

Figure 6.2 Schematic diagram of phased array focusing with a buffer consisting of a bundle of circular cylinders.

6.2 Experimental set-up and test specimen

This section describes the experiment set-up and test specimen for the imaging experiment using a PA probe with the proposed buffer consisting of a bundle of circular cylinders.

Experimental data were collected using PWI and FMC with a linear phased array probe comprising 64 elements. Each element measured 15 mm × 0.9 mm, with a pitch of 1 mm, a gap of 0.1 mm, and a total aperture of 15 mm × 63.9 mm. All elements exhibited nearly identical bandwidth characteristics, featuring a center frequency of 1.0 MHz and a full width at half maximum of approximately 1.0 MHz. The array was operated by phased array equipment (The Phased Array Company, Explorer), which incorporates a 14-bit, 64-channel architecture capable of simultaneously acquiring data from all 64 channels at a 50 MHz sampling rate. During the experiments, the system was controlled via a PC using a LabVIEW-based interface. Each PA probe element could apply a longitudinal force to the edge of its corresponding circular cylinder, injecting an ultrasonic pulse with a center frequency of 1 MHz into the paired cylinder through its dedicated piezoelectric element.

Fig. 6.3 shows a picture of the buffer consisting of a bundle of circular cylinders

used in the experiments in this section. The SUS304 circular cylinder is with 0.9 mm diameter, which is the same as the thickness of the piezo element of the PA probe, and 100 mm long, which is the same length of the stacked plate buffer investigated by numerical calculations and experiments in the previous study. Fig. 6.4 shows the end surface of the buffer. 64 circular cylinders were arranged horizontally with a 0.1 mm gap between each circular cylinder to form one layer, and the positions were fixed by curing the ends with an ultraviolet (UV) - curable adhesive of about 3 mm. This was then bonded with double-sided tape for 15 layers. Double-sided tape with a width of 5 mm and a thickness of about 0.1 mm was used at both ends of the buffer. After that, to prevent the penetration of couplant, the gaps at both ends of the buffer were filled with UV-curable adhesive. In this way, 15 circular cylinders arranged in a line can be paired with one piezoelectric element of PA probe in which way 64 piezoelectric elements can be paired with 960 circular cylinders in total, as shown in Fig. 6.4. Longitudinal wave with center frequency of 1 MHz from each piezoelectric element is applied on each circular cylinder and longitudinal mode cylinder wave which has similar vibration form as longitudinal wave, mainly propagates in the circular cylinders. Considering the dispersion curve of low fD range of 0.9 MHz mm, the longitudinal mode wave can propagate in a very low dispersion.

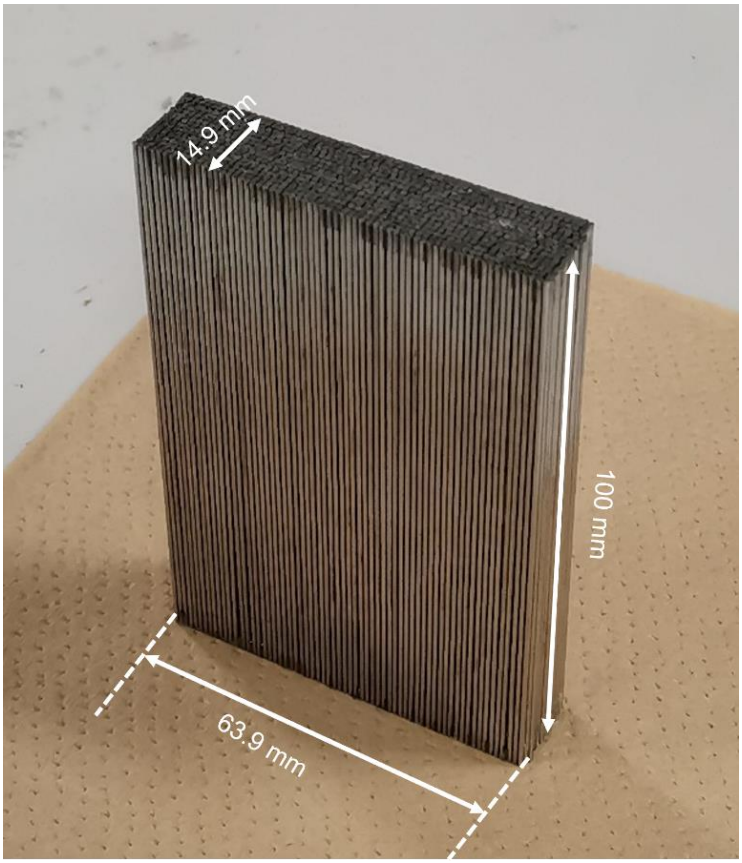

Figure 6.3 Pictures of a buffer consisting of a bundle of circular cylinders has been formed by circular cylinders.

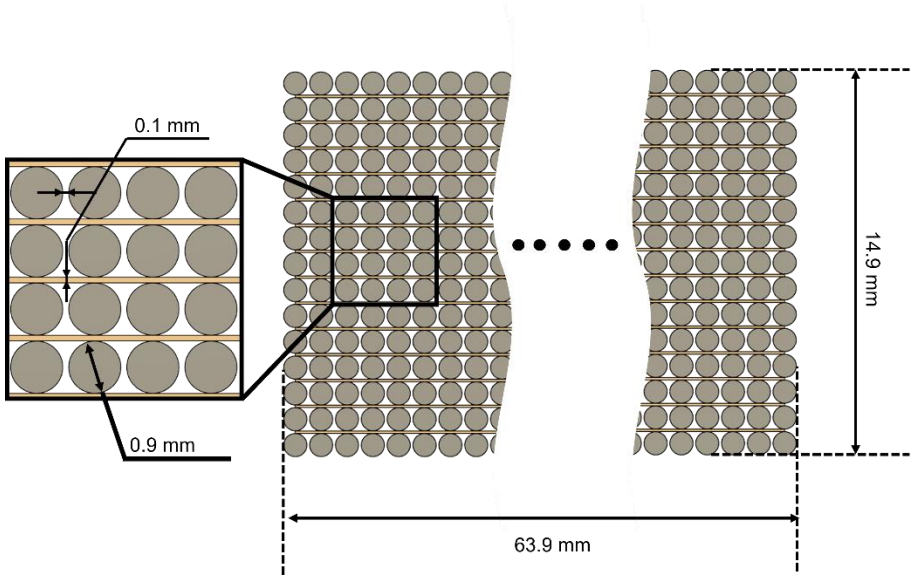

Figure 6.4 Schematic diagram of the end surface of buffer consists of a bundle of circular cylinders to show the dimensions of each component of the buffer.

As illustrated in Fig. 6.5, the aluminum alloy (A5052) specimen is a rectangular solid measuring 100 mm × 100 mm × 50 mm and contains three side-drilled holes (SDHs). The SDHs #1, #2, and #3 are positioned at depths of 20 mm, 25 mm, and 30 mm from the upper surface, and at horizontal distances of 20 mm, 40 mm, and 60 mm from the left surface, respectively. The diameters of SDHs #1 and #3 are 3.0 mm, while that of SDH #2 is 3.5 mm.

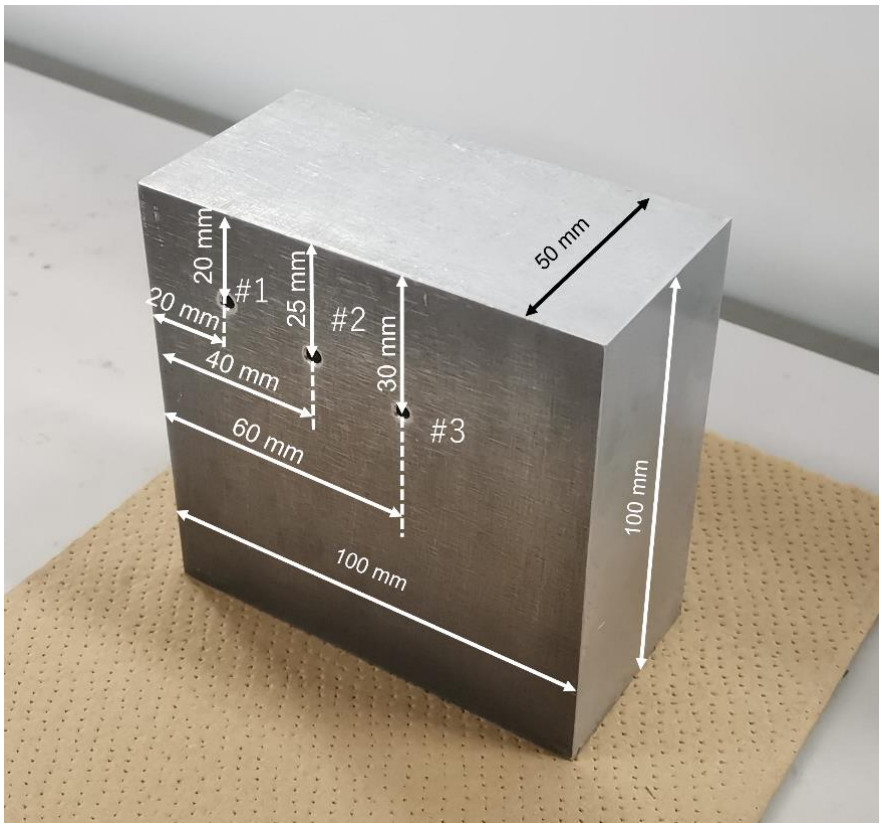

Figure 6.5 A picture of the specimen with three side-drilled holes as internal reflectors to test the effectiveness of the buffer consisting of a bundle of circular cylinders.

Waveforms were acquired and processed using two methods: PWI and FMC/TFM. For a PA probe with N elements, PWI involves the simultaneous excitation of all piezoelectric elements, with all elements recording the resulting signals. This process yields a set of $1 \times N$ waveforms. In contrast, FMC/TFM operates by having one element transmit while all elements receive echoes from the specimen. This transmit-receive cycle is repeated for each element, resulting in an $N \times N$ waveform dataset. Delay-and-sum processing based on the TFM is then applied to this dataset. The intensity at each point in the imaging region is computed using the expected delay.

Before conducting imaging experiments with the buffer consisting of a bundle of circular cylinders, the imaging test was performed using the PA probe without the buffer, as shown in Fig. 6.6(a). After confirming that the defect image could be successfully obtained with the PA probe alone, imaging was then carried out with the buffer, as shown in Fig. 6.6(b). During the experiments, a standard couplant for longitudinal waves was applied at the interfaces between the PA probe and the specimen, and between the PA probe and the buffer. For actual high-temperature inspections, a couplant or adhesive suitable for high temperature would be required. The imaging region, referred to as the region of interest (ROI), was defined as a 60 mm × 60 mm square, as shown in Fig. 6.6. The top and bottom ends of the buffer consisting of a bundle of circular cylinders were connected to the PA probe and the specimen's upper surface, respectively, with couplant applied at both contact surfaces.

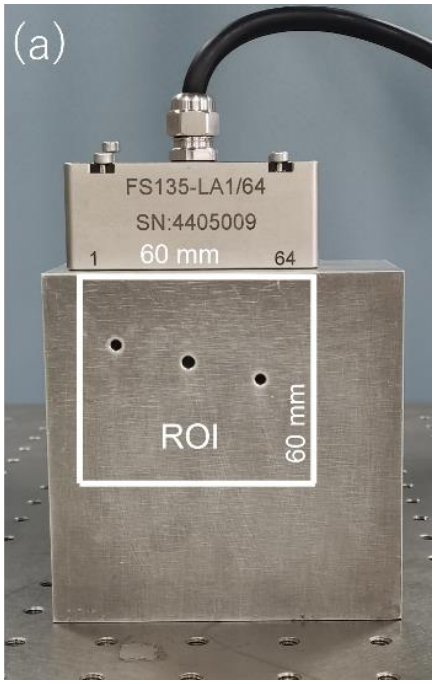

(a)

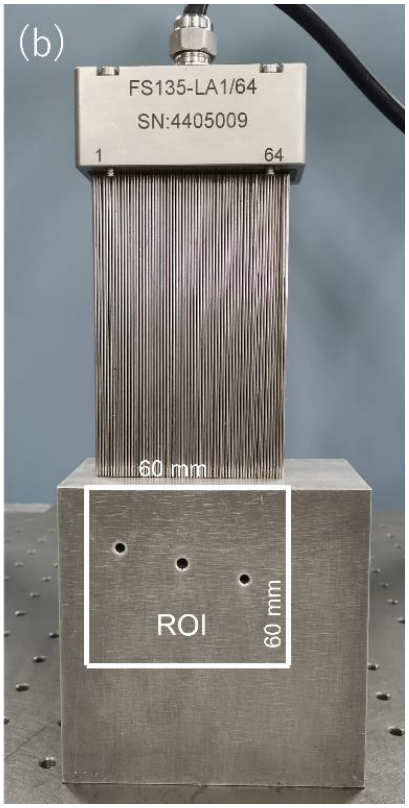

(b)

Figure 6.6 Pictures of the experimental devices and specimen when (a) phased array probe without buffer, and (b) with the buffer consisting of a bundle of circular cylinders.

6.3 Results of experiments using buffer consisting of a bundle of circular cylinders

Fig. 6.7 presents the defect images obtained in experiments using the PA probe both with and without the buffer. Defect images acquired without the buffer using PWI and FMC/TFM are shown in Fig. 6.7(a) and (b), respectively. Subsequently, defect images obtained using the PA probe with the buffer are shown in Fig. 6.7(c) and (d). These imaging procedures were carried out under the assumption that the longitudinal mode wave propagates through the buffer with a group velocity of 5060 m/s, while the longitudinal wave velocity in the aluminum specimen used in the experiment is 6200 m/s. The color scale in each image represents the intensity calculated by PWI or TFM, and all intensity values are normalized by the maximum intensity within each individual figure.

In Fig. 6.7 (a) and (b) without a buffer, clear images of three SDHs were obtained at the correct positions. When the 100 mm long buffer consisting of a bundle of circular cylinders is used, where the results are shown in Fig. 6.7 (c) and (d), the SDH images can be clearly shown at the correct positions in imaging area even with a relative higher signal-to-noise ratio (SNR) than when without buffer. Even though some noise is in the imaging area under the positions of three SDHs. There is no influence from the noise on the defect image of these SDHs because they locate in different positions from the defects.

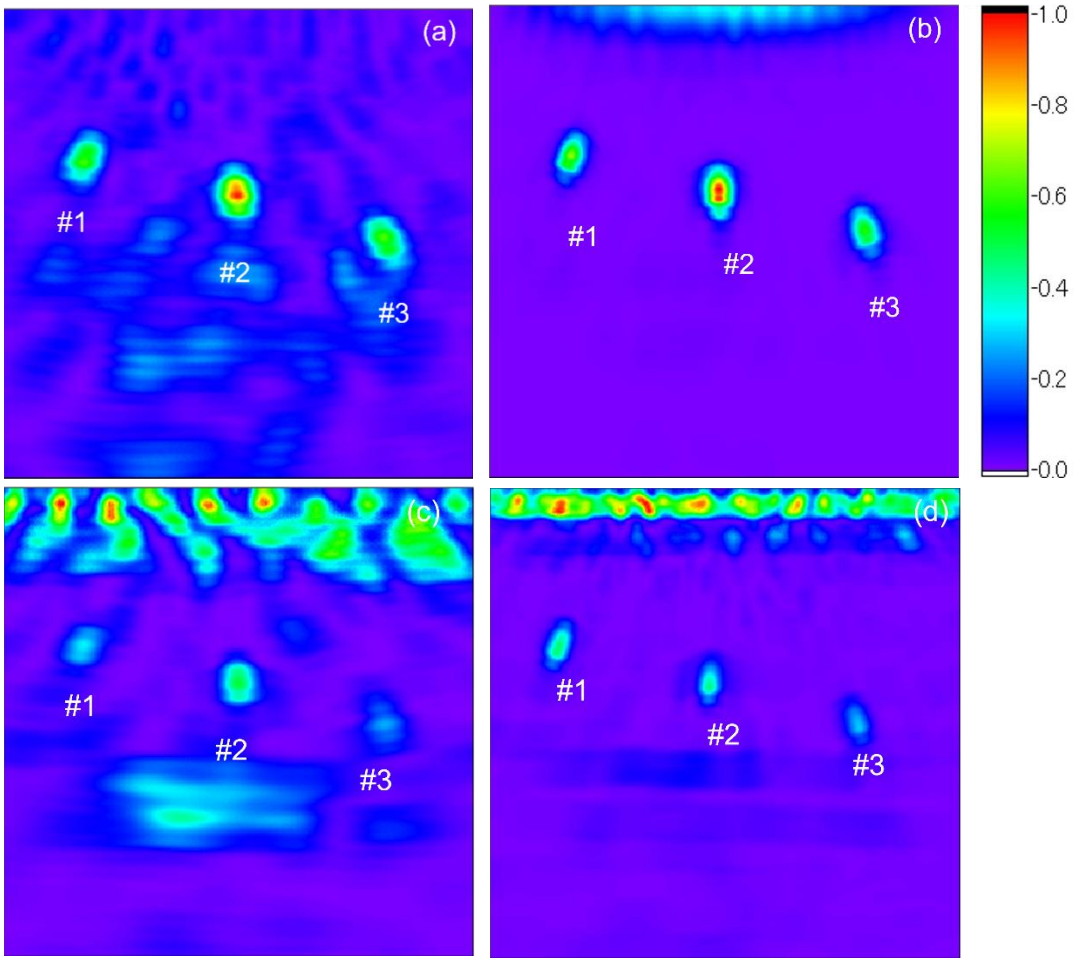

Figure 6.7 Defect images when using the PA probe with and without the buffer consisting of a bundle of circular cylinders. (a) PWI and without buffer. (b) FMC/TFM without buffer. (c) PWI with buffer. (d) FMC/TFM with buffer.

In the defect imaging results shown in Fig. 6.7, the problems of trailing wave happened in phased array imaging using a stacked plate buffer introduced in chapter 5 are successfully solved by using buffer consisting of a bundle of circular cylinders. Strictly speaking, as discussed in section 6.2, the trailing wave should be closed to the main straight wave pocket because of the small diameter, which should be shown in the upper side of the imaging area. However, the image created by trailing wave cannot be observed in these experiments using buffer consisting of a bundle of circular cylinders.

Though the problem of trailing waves has been solved by buffer consisting of a bundle of circular cylinders and the defect images can be clearly shown in the result. Some noise still appeared in the imaging area and may have some negative influence on the defect imaging. In the future work, increasing the SNR is an important object.

6.4 Summary

The feasibility of defect imaging using a PA probe attached with a buffer consisting of a bundle of circular cylinders with 0.9 mm diameter was experimentally investigated. SDHs in an aluminum specimen were imaged using a linear array probe with 64 elements with a center frequency of 1 MHz. The buffer with 100 mm length is used in the experiments. Results show that defect images can be more clearly obtained with 100 mm buffer. The imaging technique using a PA probe with the buffer consisting of a bundle of circular cylinders is expected to be used to inspect high-temperature objects and with higher SNR.

Chapter 7 Summary

7.1 Overview of the thesis

Ultrasonic PA technology is widely used in NDT and buffer is a tool for solving problems that happened when testing high temperature objects. In this thesis, buffers consist of waveguides are proposed to solve the problem of near field limit caused by bulk buffers that can prevent effective beamforming with a PA probe. Chapter 1 introduced the background of this thesis. Chapter 2 reviewed the basic theory of bulk ultrasonic waves and Lamb wave propagation in a plate. Dispersion curves of Lamb waves which are very important in following studies was presented. Chapter 3 reviewed the PA technology and explained the defect imaging method of plane wave imaging (PWI) and full matrix capture/total focusing method (FMC/TFM) which are applied in this thesis. Then, the development of the waveguide buffers was introduced from chapter 4 to chapter 6. Chapter 4 introduced the numerical investigation on phased array imaging with a stacked plate buffer. Chapter 5 followed the previous chapter and experimentally investigated the validation of the phased array imaging with a stacked plate buffer but found the problem caused by trailing wave even though solve the problem by extending the width of the buffer plate. For solving the problem from trailing wave, a buffer consisting of circular cylinders was proposed in chapter 6.

7.2 Summary of findings in this thesis

In chapter 4, numerical simulations were conducted to evaluate PA imaging performance using a stacked plate buffer, which was designed based on the dispersion characteristics of the S0 Lamb wave mode to maintain the performance of the phased array transducer. Initial results of simulations revealed limitations in imaging quality due to multiple reflections at the buffer ends. The concept of the effective detecting region (EDR) for a PA probe with a stacked plate buffer was proposed and theoretically derived. Numerical calculation results confirmed the agreement between theoretical predictions and simulation results. It was further demonstrated that increasing the buffer length led to an extension of the EDR.

In chapter 5, experimental investigations were performed to evaluate the feasibility of PA imaging with the stacked plate buffer. A buffer fabricated in accordance

with the S0 mode dispersion was used in defect imaging experiments. Initial experimental results exhibited strong spurious signals and blurred defect images. Follow-up numerical analyses attributed these artifacts to trailing waves generated in the thin plates. Theoretical and numerical investigations indicated that increasing the plate width could effectively remove these trailing waves. Experiments with wider plates confirmed that the spurious images were effectively removed, yielding significantly clearer defect images.

In chapter 6, to further solve the problems of trailing waves, a buffer consisting of thin circular cylinders was introduced. The design was determined by considering the dispersion characteristics of the longitudinal guided wave mode in circular cylinders and parameters of the PA probe. Experimental results demonstrated successful defect imaging using both PWI and TFM, even under relatively low SNR conditions. The influences of trailing waves happened in stacked plate buffer were successfully solved by thin circular cylinder buffer with small diameter.

7.3 Recommendation for future work

Even though the object is for testing high temperature with about 500 ℃, in the research introduced in this thesis, all the numerical calculations and experiments are set to be in the room temperature. In this thesis, the validation of the buffer consist of waveguide has been investigated and this method has been proved to be a possible solution for PA probe to test a high temperature object. For the next step, the research for testing the feasibility of PA imaging with buffer consists of waveguide for high temperature object testing can be conducted and some of the points should be considered.

The method of attachment of the waveguides should be considered. The methods for attaching the waveguides to be a buffer in this thesis may be only able to use in room temperature. For instance, in the experiment of stacked plate buffer, the plates are attached by double-sided tape. However, in high temperature about 500℃, the tapes used in the experiment in room temperature may not be used. Thus, a new method of attachment appropriate in high temperature should be found.

The heat transfer in waveguide buffer and the dissipation of the buffer should be considered. In the research introduced in this thesis, numerical calculations are assumed to be in condition of room temperature and all the experiments are conducted in room temperature. The influence of heat transferring inside the buffer is not considered. In the future work, the specimen will be with a relatively high temperature. Thus, we need to

consider the cooling method for the waveguide buffer. The structure of the waveguide buffer now we have can be hard for dissipation because the waveguides are close to each other and assembled to be a cluster. The outer waveguides will dissipate heat more easily than the inner waveguides. Thus, for the structure of the buffer, the buffer should be designed to be easy for dissipation.

References

1. Rodríguez, D. A. Lozano Tafur, C. Melo Daza, P. F. Villalba Vidales, J. A. Daza Rincón, J. C. Inspection of aircrafts and airports using UAS: A review. *Results in Engineering* **22**, 102330 (2024).

2. Guo, F. Liu, J. Zou, F. Wang, Z. Aircraft assembly quality control with feedback actions and assembly station flowing fluctuation analysis. *IEEE Access* **8**, 190118–190135 (2020).

3. Scherer, W. T. Glagola, D. M. Markovian models for bridge maintenance management. *Journal of Transportation Engineering* **120**, 37–45 (1994).

4. Lee, S. H. Choi, S. W. Lee, E. B. A question-answering model based on knowledge graphs for the general provisions of equipment purchase orders for steel plants maintenance. *Electronics* **12**(11), 2504 (2023).

5. Hafizi, M. Jamaludin, S. N. S. Shamil, A. H. State of the art review of quality control method in automotive manufacturing industry. *IOP Conference Series: Materials Science and Engineering* **530**, 012034 (2019).

6. Somvanshi, U. Quality control in automobile manufacturing industries. *International Journal for Research in Applied Science and Engineering Technology* **8**, 740–750 (2020).

7. Khan, F. I. Haddara, M. Risk-Based Maintenance (RBM): A new approach for process plant inspection and maintenance. *Process Safety Progress* **23**, 252–265 (2004).

8. Wayan Ngarayana, I. Do, T. M. D. Murakami, K. Suzuki, M. Nuclear power plant maintenance optimisation: models, methods & strategies. *Journal of Physics: Conference Series* **1198**, 022005 (2019).

9. Nguyen, D. Bagajewicz, M. Optimization of preventive maintenance in chemical process plants. *Industrial & Engineering Chemistry Research* **49**, 4329–4339 (2010).

10. Ballesteros, A. Sanda, R. Maqua, M. Stephan, J. L. Maintenance related events in nuclear power stations. *Maintenance and Reliability* **19**(1), 26–30 (2017).

11. Hüthwohl, P. Lu, R. Brilakis, I. O'rourke, L. Challenges of bridge maintenance inspection, *International Conference on Computing in Civil and Building Engineering*, Osaka, Japan, July 6–8 (2016).

12. Wang, B. Zhong, S. Lee, T. L. Fancey, K. S. Mi, J. Non-destructive testing and evaluation of composite materials/structures: A state-of-the-art review. *Advances in Mechanical Engineering* **12**(4), 1–28 (2020).

13. Lopez, A. Bacelara, R. Piresa, I. Santosb, T. G. Sousac, J. P. Quintino, Luísa. Non-destructive testing application of radiography and ultrasound for wire and arc additive manufacturing. *Additive Manufacturing* **21**, 298–306 (2018).

14. Qu, Z. Jiang, P. Zhang, W. Development and application of infrared thermography non-destructive testing techniques. *Sensors* **20**(14), 3851 (2020).
15. Menaria, T. Kumar, M. Radiographic imaging modalities for non-destructive testing and evaluation (NDT & E)*, Proceedings of International Conference on Sustainable Computing in Science, Technology and Management (SUSCOM),* Jaipur, India, February 26–28, (2019).
16. Inês Silva, M. Malitckii, E. Santos, T. G. Vilaça, P. Review of conventional and advanced non-destructive testing techniques for detection and characterization of small-scale defects. *Progress in Materials Science*. **138**, 101155 (2023).
17. Khedmatgozar Dolati, S. S. Caluk, N. Mehrabi, A. Khedmatgozar Dolati, S. S. Non-destructive testing applications for steel bridges. *Applied Sciences* **11**(20), 9757 (2021).
18. Kumar, A. Arnold, W. High resolution in non-destructive testing: A review. *Journal of Applied Physics* **132**(10), 100901 (2022).
19. Umar, M. Z. Vavilov, V. Abdullah, H. Ariffin, A. K. Ultrasonic infrared thermography in non-destructive testing: A review. *Russian Journal of Nondestructive Testing* **52**(4), 212–219 (2016).
20. Raišutis, R. Jasiūnienė, E. Šliteris, R. Vladišauskas, A. The review of non-destructive testing techniques suitable for inspection of the wind turbine blades. *Ultrasound* **63**(1), 26–30 (2008).
21. Zhu, J. Mao, Z. Wu, D. Zhou, J. Jiao, D. Shi, W. Zhu, W. Liu, Z. Progress and trends in non-destructive testing for thermal barrier coatings based on tnfrared thermography: A review. *Journal of Nondestructive Evaluation* **41**(3), 49 (2022).
22. Usamentiaga, R. Venegas, P. Guerediaga, J. Vega, L. Molleda, J. Bulnes, F.G. Infrared thermography for temperature measurement and non-destructive testing. *Sensors* **14**(7), 12305–12348 (2014).
23. Sultan, R. Guirguis, S. Younes, M. El-Soaly, E. Active infrared thermography technique for the non destructive testing of composite material. *International Journal of Mechanical Engineering and Robotics Research,* **1**(3), 131–142 (2012).
24. Ulus, Ö., Davarcı, F. E. Gültekin, E. E. Non-destructive testing methods commonly used in aviation. *International Journal of Aeronautics and Astronautics* **5**(1), 10–22 (2024).
25. Kumar, S. Mahto, D. Recent trends in industrial and other engineering applications of non-destructive testing: A review. *International Journal of Scientific & Engineering Research* **4**(9), 183–195 (2013).
26. Deepak, J. R. Bupesh Raja, V. K. Srikanth, D. Surendran, H. Nickolas, M. M. Non-destructive testing (NDT) techniques for low carbon steel welded joints: A review and

experimental study. *Materials Today: Proceedings*. **44**(5), 3732–3737 (2021).
27. Dwivedi, S. K. Vishwakarma, M. Soni, A. Advances and researches on non destructive testing: A review. *Materials Today: Proceedings* **5**(2), 3690–3698 (2018).
28. Ciecieląg, K. Kęcik, K. Skoczylas, A. Matuszak, J. Korzec, I. Zaleski, R. Non-destructive detection of real defects in polymer composites by ultrasonic testing and recurrence analysis. *Materials* **15**(20), 7335 (2022).
29. Honarvar, F. Varvani Farahani, A. A review of ultrasonic testing applications in additive manufacturing: Defect evaluation, material characterization, and process control. *Ultrasonics* **108**, 106227 (2020).
30. Schabowicz, K. Non-destructive testing of materials in civil engineering. *Materials* **12**, 1–13 (2019).
31. Zhang, J. Cho, Y. Kim, J. Malikov, A.K.u. Kim, Y.H. Yi, J.H. Li, W. Non-destructive evaluation of coating thickness using water immersion ultrasonic testing. *Coatings* **11**(11), 1421 (2021).
32. Jasiūnienė, E. Mažeika, L. Samaitis, V. Cicėnas, V. Mattsson, D. Ultrasonic non-destructive testing of complex titanium/carbon fibre composite joints. *Ultrasonics* **95**, 13–21 (2019).
33. Chris Roshan, C., Vasanth Ram, H. Solomon, J. Non-destructive testing by liquid penetrant testing and ultrasonic testing-a review. *International Journal of Advance Research* **5**(2), 694–697 (2019).
34. Green, R. E. Non-contact ultrasonic techniques. *Ultrasonics* **42**, 9–16 (2004).
35. Jodhani, J. Handa, A. Gautam, A. Ashwni. Rana, R. Ultrasonic non-destructive evaluation of composites: A review. *Materials Today: Proceedings* **78**(3), 627–632 (2023).
36. El Kouche, A. Hassanein, H. S. Ultrasonic non-destructive testing (NDT) using wireless sensor networks. *Procedia Computer Science* **10**, 136–143 (2012).
37. Reddy, K. A. Non-destructive testing, evaluation of stainless steel materials. *Materials Today: Proceedings* **4**(8), 7302–7312 (2017).
38. Carvalho, A. A., Rebello, J. M. A., Souza, M. P. V. Sagrilo, L. V. S. Soares, S. D. Reliability of non-destructive test techniques in the inspection of pipelines used in the oil industry. *International Journal of Pressure Vessels and Piping* **85**(11), 745–751 (2008).
39. Satyanarayan, L. Sridhar, C. Krishnamurthy, C. V. Balasubramaniam, K. Simulation of ultrasonic phased array technique for imaging and sizing of defects using longitudinal waves. *International Journal of Pressure Vessels and Piping* **84**(12), 716–729 (2007).
40. Bazulin, E. G. Comparison of systems for ultrasonic nondestructive testing using antenna arrays or phased antenna arrays. *Russian Journal of Nondestructive Testing* **49**(7), 404–423 (2013).

41. Lei, X. Wirdelius, H. Rosell, A. Experimental validation of a phased array probe model in ultrasonic inspection. *Ultrasonics* **108**, 106217 (2020).
42. Wang, X. Li, W. Li, Y. Zhou, Z. Zhang, J. Zhu, F. Miao, Z. Phased array ultrasonic testing of micro-flaws in additive manufactured titanium block. *Materials Research Express* **7**, 016572 (2020).
43. Yuan, C. Xie, C. Li, L. Zhang, F. Gubanski, S. M. Ultrasonic phased array detection of internal defects in composite insulators. *IEEE Transactions on Dielectrics and Electrical Insulation* **23**, 525–531 (2016).
44. Drinkwater, B. W. Wilcox, P. D. Ultrasonic arrays for non-destructive evaluation: A review. *NDT and E International* **39**, 525–541 (2006).
45. Chatillon, S. Cattiaux, G. Serre, M. Roy, O. Ultrasonic non-destructive testing of pieces of complex geometry with a flexible phased array transducer. *Ultrasonics* **38**, 131–134 (2000).
46. Mcnab, A. Campbell, M. J. Ultrasonic phased arrays for nondestructive testing. *NDT international* **20**(6), 333–337 (1987).
47. Kawanami, S. Kurokawa, M. Taniguchi, M. Tada, Y. Development of phased-array ultrasonic testing probe, *Mitsubishi Juko Giho* **38**(3), 154–157 (2001).
48. Lozonschi, L. T. Panaite, C. E. Safety analysis of thermal equipment and piping systems in the CANDU nuclear power plant subjected to thermal shocks. *IOP Conference Series: Materials Science and Engineering* **1262**, 012082 (2022).
49. Tamura, A. A Review: Recent Advances in Pipe-Wall Thinning Inspection Technologies in Nuclear Power Plants. *Journal of Flow and Energy* **2**, 118–135 (2024).
50. Sandhu, H. K. Srikanth Bodda, S. Sauers, S. Gupta, A. Condition monitoring of nuclear equipment-piping using deep learning. *International Conference on Structural Mechanics in Reactor Technology* Berlin, Germany, 20–24 September (2022).
51. Luo, Y. Gu, W. Peng, W. Jin, Q. Qin, Q. Yi, C. A study on microstructure, residual stresses and stress corrosion cracking of repair welding on 304 stainless steel: Part I-Effects of heat input. *Materials* **13**(10), 2416 (2020).
52. Lozonschi, L. T. Panaite, C. E. Safety analysis of thermal equipment and piping systems in the CANDU nuclear power plant subjected to thermal shocks. *IOP Conference Series: Materials Science and Engineering* **1262**, 012082 (2022).
53. Fan, E., Li, Y. Lv, X. A study on the stress corrosion mechanism of microstructures in a heat-affected zone of high-strength steel weldment in artificial seawater. *Surface Topography: Metrology and Properties* **9**, 025040 (2021).
54. Yu, L. Liu, Y. Deng, H. Zhang, S. Wang, Y. Zhou, Y. Cracking Failure Analysis of Pipe to Flange Weld Joint. *Conference Series: Earth and Environmental Science* **859**,

012012 (2021).
55. Khodamorad, S. H., Alinezhad, N., Haghshenas Fatmehsari, D. Ghahtan, K. Stress corrosion cracking in Type.316 plates of a heat exchanger. *Case Studies in Engineering Failure Analysis* **5–6**, 59–66 (2016).
56. Zumpano, G. Meo, M. A new nonlinear elastic time reversal acoustic method for the identification and localisation of stress corrosion cracking in welded plate-like structures - A simulation study. *International Journal of Solids and Structures* **44**(11-12), 3666–3684 (2007).
57. Li, C. Analysis of piping and support weld defects of VVP system in nuclear power plant and study on treatment measures. *Journal of Physics: Conference Series*. **2338**, 012009 (2022).
58. Takaya, S. Miya, K. Application of magnetic phenomena to analysis of stress corrosion cracking in welded part of stainless steel. *Journal of Materials Processing Technology* **161**, 66–74 (2005).
59. Yin, Q. Feng, H. Xue, D. Shu, G. A special thermal fatigue failure mode of pipe in nuclear power plant and its countermeasures. *Journal of Physics: Conference Series* **1885,** 032063 (2021).
60. Kobayashi, M. Jen, C. K. Bussiere, J. F. Wu, K. T. High-temperature integrated and flexible ultrasonic transducers for nondestructive testing. *NDT and E International* **42**(2), 157–161 (2009).
61. Kažys, R. Voleišis, A. Baršauskas, V. High temperature ultrasonic transducers: Review. *Ultrasound* **63**(2), 7–17 (2008).
62. Maznev, A.A. Wright, O.B. Upholding the diffraction limit in the focusing of light and sound. *Wave motion* **68,** 182–189 (2017).
63. Monemi, M. Bahrami, S. Rasti, M. Latva-Aho, M. A study on characterization of near-field sub-regions for phased-array antennas. *IEEE Transactions on Communications* **73**(5), 2964–2979 (2025).
64. Monemi, M. Rasti, M. Latva-aho, M. Revisiting the Fraunhofer and Fresnel boundaries for phased array antennas. *IEEE Global Communications Conference* 4744–4749 (2024).
65. Sun, Y. Zhang, Y. Qian, C. Zhang, Z. Near-field ultrasonic phased array deflection focusing based CFRP wing box structural health monitoring. *International Journal of Distributed Sensor Networks* **2013**(4), 1–6 (2013).
66. Fukuchi, T. Hayashi, T. Mori, N. Ultrasonic focusing using a stacked thin-plate region. *Japanese Journal of Applied Physics* **62**, SJ1005 (2023).
67. Joseph, L. R. Ultrasonic waves in solid media. Cambridge University Press, (2014).

68. Graff, K, F. Wave motion in elastic solids, Ohio State University Press, (1975).
69. Dwivedi, S. K. Vishwakarma, M. Soni, A. Advances and researches on non destructive testing: A review. *Materials Today: Proceedings* **5**(2), 3690–3698 (2018).
70. 林高弘, 超音波による非破壊材料評価の基礎, 大阪大学出版, (2021)
71. Hayashi, T. Song, W. J. Rose, J. L. Guided wave dispersion curves for a bar with an arbitrary cross-section, a rod and rail example. *Ultrasonics* **41**, 175–183 (2003).
72. Naqvi, A. H. Lim, S. Review of recent phased arrays for millimeter-wave wireless communication. *Sensors* **18**(10), 3194 (2018).
73. Li, M. Chen, S. L. Liu, Y. Guo, Y. J. Wide-angle beam scanning phased array antennas: A review. *IEEE Open Journal of Antennas and Propagation* **4**, 695–712 (2023).
74. Wei, Y. Review of the evolution of phased-array radar. *SHS Web of Conferences* **144**, 02008 (2022).
75. He, C. Zhang, X. Lu, Y. Wu, B. Lee, Y. Sound fields radiated from a linear phased array based on analytical solutions of transient elastic waves. *Wave Motion* **73**, 86–95 (2017).
76. Le Jeune, L. Robert, S. Lopez Villaverde, E. Prada, C. Jeune, L. LE. Plane wave imaging for ultrasonic non-destructive testing: Generalization to multimodal imaging, *Ultrasonics* **64**, 128–138 (2016).
77. Redwood M. Narrow-bandwidth pulses in solid waveguides. Mechanical Waveguides, New York: Pergamon Press, p. 190–207 (1960).

Research achievements

Peer reviewed papers

1. Xia, M. Hayashi, T. Mori, N. Numerical analysis of the phased array imaging with a stacked plate buffer. *Japanese Journal of Applied Physics* **63**, 03SP55 (2024).

2. Xia, M. Hayashi, T. Mori, N. Experimental investigation of defect imaging using a phased array probe with a stacked plate buffer. *NDT & E International* **151**, 103316 (2025).

Conference presentations

1. Xia, M. Fukuchi, T. Hayashi, T. Mori, N.
"Control of guided wave propagation with layered path in a plate"
The 43th Symposium on Ultrasonic Electronics (USE2022).
Kyoto, Japan, Nov. 2022

2. Xia, M. Hayashi, T. Mori, N.
"Defect imaging using a phased array transducer with a stacked plate buffer"
International Congress on Ultrasonics (ICU2023).
Beijing, China, Sep. 2023

3. Xia, M. Hayashi, T. Mori, N.
"Phased array imaging with a stacked plate buffer"
The 44th Symposium on Ultrasonic Electronics (USE2023).
Toyama, Japan, Nov. 2023

4. Xia, M. Hayashi, T. Mori, N.
"Thin waveguide buffer for insulating an ultrasonic probe from hot and cold temperature"
World Conference on Non-Destructive Testings (WCNDT2024).
Incheon, Korea, May 2024